

Fizeau drag in graphene plasmonics

<https://doi.org/10.1038/s41586-021-03640-x>

Received: 6 October 2020

Accepted: 12 May 2021

Published online: 23 June 2021



Y. Dong^{1,2,6}, L. Xiong^{1,6}, I. Y. Phinney³, Z. Sun¹, R. Jing¹, A. S. McLeod¹, S. Zhang¹, S. Liu⁴, F. L. Ruta^{1,2}, H. Gao³, Z. Dong³, R. Pan¹, J. H. Edgar⁴, P. Jarillo-Herrero³, L. S. Levitov³, A. J. Millis¹, M. M. Fogler⁵, D. A. Bandurin^{3✉} & D. N. Basov^{1✉}

Dragging of light by moving media was predicted by Fresnel¹ and verified by Fizeau's celebrated experiments² with flowing water. This momentous discovery is among the experimental cornerstones of Einstein's special relativity theory and is well understood^{3,4} in the context of relativistic kinematics. By contrast, experiments on dragging photons by an electron flow in solids are riddled with inconsistencies and have so far eluded agreement with the theory^{5–7}. Here we report on the electron flow dragging surface plasmon polaritons^{8,9} (SPPs): hybrid quasiparticles of infrared photons and electrons in graphene. The drag is visualized directly through infrared nano-imaging of propagating plasmonic waves in the presence of a high-density current. The polaritons in graphene shorten their wavelength when propagating against the drifting carriers. Unlike the Fizeau effect for light, the SPP drag by electrical currents defies explanation by simple kinematics and is linked to the nonlinear electrodynamics of Dirac electrons in graphene. The observed plasmonic Fizeau drag enables breaking of time-reversal symmetry and reciprocity¹⁰ at infrared frequencies without resorting to magnetic fields^{11,12} or chiral optical pumping^{13,14}. The Fizeau drag also provides a tool with which to study interactions and nonequilibrium effects in electron liquids.

Graphene offers an ideal medium^{15–18} for observing the plasmonic Fizeau drag, as it supports the propagation of highly confined, long-lived and electrically tunable SPPs. Crucially, graphene also withstands ultrahigh current densities (of the order of $\text{mA } \mu\text{m}^{-1}$)¹⁹ so that the carrier drift velocity u can be comparable to the SPP group velocity. In the absence of current, the SPP dispersion follows $\omega(-q) = \omega(q) \propto \sqrt{q}$ (Fig. 1a), where ω and q are the frequency and wavevector of the SPPs, respectively. Under applied direct current, the SPP dispersion is predicted to depend^{20–24} on the relative orientation of SPP propagation and carrier flow, generating the plasmonic Fizeau effect that breaks the reciprocity of the system: $\omega(-q) \neq \omega(q)$. Here we report on exploiting the unique attributes of graphene to demonstrate the physics of the plasmonic Fizeau effect where SPPs are dragged by drifting Dirac electrons. After completing this work, we became aware of similar results by W. Zhao et al.²⁵

To explore the plasmonic Fizeau drag, we fabricated multi-terminal graphene devices schematically shown in Fig. 1b. Monolayer graphene (MLG) encapsulated in hexagonal boron nitride (hBN) was integrated into back-gated structures assembled on a Si/SiO₂ substrate (285 nm of oxide). Gold SPP launchers^{16,18} were deposited directly on the graphene among drain electrodes such that the current-gating effect²⁶ (see Methods sections 'Gate-dependent transport' and 'Current-gating effects') from spatial inhomogeneity of electron density n was minimized. The gold launcher also served as an Ohmic contact to the graphene and as a heat sink for electrons in our high-current experiments. Finally, the width of the current-carrying graphene channel was narrowed down to 2 μm to boost the local current density and

enhance the Fizeau drag effect. Real-space SPP images were acquired using low-temperature near-field optical nanoscopy techniques. An infrared laser of frequency ω illuminated the gold launcher (Fig. 1b), which excited propagating SPPs. The SPP electric field was out-coupled by a metallized tip of an atomic force microscope into free-space photons and subsequently registered by a detector. Using the demodulated detector signal, the real-space profiles of SPPs were reconstructed^{16–18}. The experiments were performed at cryogenic temperatures to reduce phonon-induced losses¹⁸ and thus improve the fidelity of the measurements.

We now describe how the frequency–momentum dispersion $\omega(q)$ of SPPs is affected by the electric current in the graphene channel. The direct observable of our nano-imaging experiments is the wavelength λ_p of SPPs, which is related to the real part of the SPP wavevector, $q_1 = 2\pi/\lambda_p$ ($q = q_1 + iq_2$). In realistic graphene devices, the square-root law of SPP dispersion is modified by phonon resonances in the hBN substrate^{16–18} but the dispersion relation $\omega(q)$ remains $q/-q$ symmetric. Under applied direct current (d.c.) with density J_{dc} , the Dirac electrons supporting SPPs in graphene acquire a drift velocity $u = J_{dc}/en$, where e is the elementary charge and n is the carrier density. The drifting carriers were predicted^{20–24} to induce a plasmonic Fizeau effect, which leads to an increase in λ_p when SPPs co-propagate with the carriers (Fig. 1a, right branch) and a decrease in λ_p for the counter-propagation scenario (Fig. 1a, left branch). Our detailed theory (Supplementary Information) corroborates this intuition but reveals additional complications. Specifically, the drifting carriers modify the electromagnetic response of the system in a quasi-relativistic way^{20,27} with the Lorentz

¹Department of Physics, Columbia University, New York, NY, USA. ²Department of Applied Physics and Applied Mathematics, Columbia University, New York, NY, USA. ³Department of Physics, Massachusetts Institute of Technology, Cambridge, MA, USA. ⁴The Tim Taylor Department of Chemical Engineering, Kansas State University, Manhattan, KS, USA. ⁵Department of Physics, University of California San Diego, La Jolla, CA, USA. ⁶These authors contributed equally: Y. Dong, L. Xiong. ✉e-mail: bandurin.d@gmail.com; db3056@columbia.edu

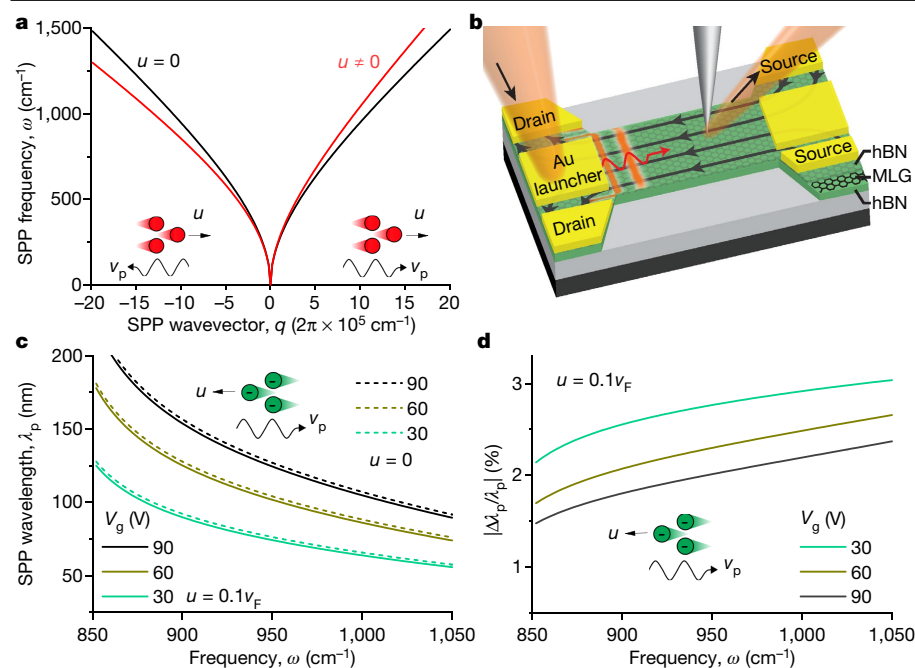


Fig. 1 | Plasmonic Fizeau drag in graphene: theory and modelling. **a**, Theoretical SPP dispersion with (red line) and without (black line) drifting carriers. Carrier density is $n = 1 \times 10^{11}$ cm⁻² and the non-zero drift velocity is $u = 0.7v_F$ with $+u$ along the $+q$ direction. Wavy black arrows indicate the SPP propagation direction and straight black arrows represent the carrier drift direction. **b**, Schematic of a graphene device with a constricted channel. Under the illumination of an infrared laser, the gold launcher excites propagating SPPs, which were visualized by near-field tip-based imaging techniques. Black streamlines represent carrier drift directions. **c**, The SPP wavelength λ_p as a function of the laser frequency ω with (solid lines, $u = 0.1v_F$) and without (dashed lines, $u = 0$) current at different gate voltages V_g . The SPP wavelength is diminished under drifting current. **d**, The Fizeau shift $|\Delta\lambda_p/\lambda_p|$ as a function of the laser frequency ω at different gate voltages V_g for a typical drift velocity $u = 0.1v_F$.

factor $\gamma = (1 - u^2/v_F^2)^{-1/2}$, where v_F is the graphene Fermi velocity. In addition, the corrections of Fizeau shift in the second order of the drift velocity are not negligible and prompt nonlinearities discussed below.

Next, we explore the experimental parameter space of the plasmonic Fizeau effect by modelling the wavelength shift $\Delta\lambda_p/\lambda_p$ for our device at different gate voltages V_g , laser frequencies ω and drift velocities u (Fig. 1c, d). Assuming a drift velocity of $u = 0.1v_F$, a value readily achievable in our structures, the SPP wavelength is shortened compared to $u = 0$ for plasmons counter-propagating with carriers (solid and dashed lines in Fig. 1c). The magnitude of the Fizeau shift $\Delta\lambda_p/\lambda_p$ increases at higher laser frequency ω and lower gate voltage V_g (Fig. 1d). Choosing the lowest gate voltage $V_g = 30$ V seems favourable for generating the largest Fizeau shift. However, both the amplitude and the propagation length of SPPs rapidly diminish at low V_g , compromising the fidelity of the experimental data. Higher laser frequency also results in similar adverse effects. We therefore chose to conduct the measurement at $\omega = 890$ cm⁻¹ and a moderate gate voltage $V_g = 47$ V, corresponding to a carrier density $n = 2.9 \times 10^{12}$ cm⁻².

We next analyse the experimental evidence for the plasmonic Fizeau effect (Fig. 2), acquired from a representative device shown in Fig. 2a. Near-field signals were acquired at $T = 170$ K and $V_g = 47$ V by repeatedly scanning along the same line perpendicular to the launching edge while varying the current density. Individual line scans were assembled into a two-dimensional false-colour plot with position on the horizontal axis and current density on the vertical axis (Fig. 2b). In this representation, SPPs were excited by the gold launcher on the left of the field of view and propagated to the right, manifesting themselves as periodic oscillations^{16–18} of the scattering amplitude signal (Fig. 2b). Somewhat enhanced plasmonic loss can be observed at the largest applied current densities, which is caused by Joule heating. In Fig. 2c, we show line profiles averaged over a range of ± 25 $\mu\text{A } \mu\text{m}^{-1}$ extracted from Fig. 2b at different current densities. Damped sinusoidal functions were used to fit (Methods section ‘Fitting method’) the experimental data and the fitting results are displayed along with the raw data points (Fig. 2c). Experimental line profiles at different current densities show a smooth evolution of the SPP wavelength with current density. For positive current densities, electrons flow towards the launcher and SPPs propagate away from the launcher. The counter-propagation of electrons and plasmons results in a clear reduction of the SPP wavelength, as evident from the comparison of the fitting results in Fig. 2d. The observed wavelength

downshift is consistent with the $q < 0$ dispersion branch in Fig. 1a where the SPP wavevector q is enlarged in the counter-propagation setting. Notably, the wavelength minimally increased upon current polarity reversal, owing to the second-order correction to the Fizeau effect described below. We acquired data from multiple devices at 170 K and 60 K (Extended Data Fig. 7) which all showed the same trends as in Fig. 2b–d. The fact that the SPP wavelength depends on current polarity suggests that the SPP Fizeau effect breaks the $q/-q$ reciprocity in our nano-plasmonic device.

Having established qualitative indicators of the plasmonic Fizeau drag, we now examine the findings quantitatively. We fit every line profile (Methods sections ‘Fitting method’ and ‘Monte Carlo simulation of regression coefficients’) in datasets such as Fig. 2b and obtained the Fizeau shift $\Delta\lambda_p/\lambda_p$ as a function of current density J_{dc} and drift velocity u (Fig. 3a, b). The results reveal that the Fizeau shift reaches $\sim 2.5\%$ at $J_{dc} = 0.7$ mA μm^{-1} for the counter-propagation setting (Fig. 3a). For the co-propagation setting, the Fizeau shift is very small and shows nonlinear dependence on drift velocity. When reversing the polarity of the gate voltage, which switches the carrier type to holes, the observed dependence of Fizeau shift on hole drift velocity was similar to that for electrons (Fig. 3b). These observations indicate an ambipolar character of the Fizeau drag, which depends on the carrier drift velocity but not on the carrier type.

Discussion

A salient feature of the experimental data is that the Fizeau shifts in Fig. 3a, b are neither symmetric with the current direction nor linearly varying with the carrier drift velocity. The observed experimental trends can be understood based on a model which accounts for both linear and quadratic terms of the Fizeau shift as a function of $u \ll v_F$:

$$\frac{\Delta\lambda_p}{\lambda_p} = \eta \frac{u}{v_g} - \left(\eta + \frac{1}{4} \right) \frac{v_p}{2v_g} \frac{u^2}{v_F^2}, \quad v_p = \frac{\omega\lambda_p}{2\pi}, \quad (1)$$

where η is the drag coefficient and v_p is the plasmon phase velocity. Note that $v_g \approx 1/2v_p$ reduces to the plasmon group velocity only when the dielectric screening is nondispersive. In our device, the screening from hBN boosts the magnitude of the Fizeau shift by suppressing v_g . The drag coefficient η assumes a value in the interval $1/4 \leq \eta \leq 1/2$ depending

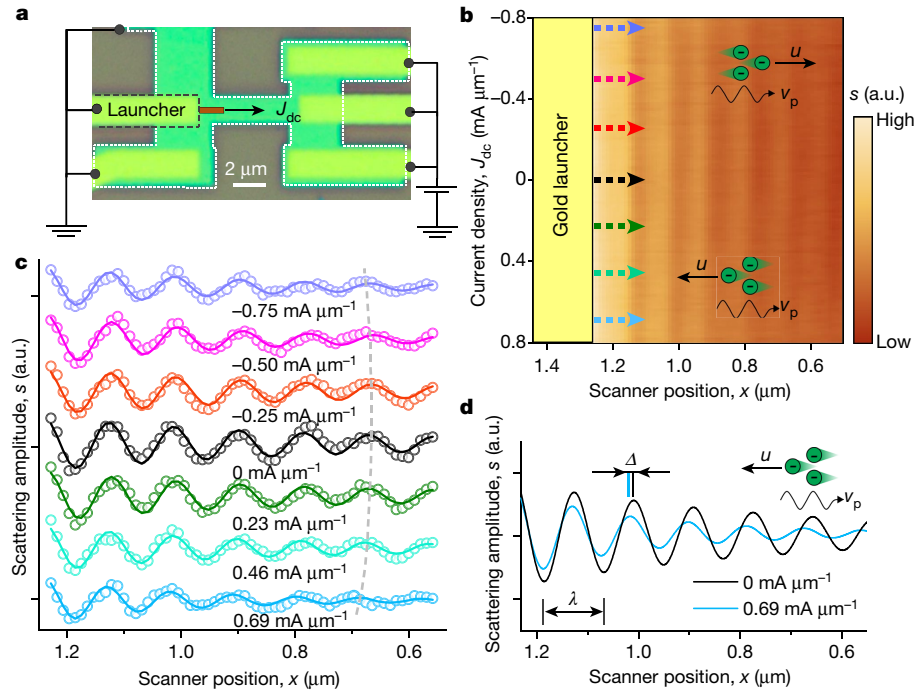


Fig. 2 | Experimental demonstration of the plasmonic Fizeau drag. **a**, An optical image of a representative device. Yellow leads are gold contacts to graphene; green region corresponds to graphene encapsulated between hBN slabs. Data displayed in **b–d** were collected in the dark red region while scanning along a single line. The black arrow represents positive current direction. **b**, Near-field image, at $V_g = 47$ V and $T = 170$ K, acquired by scanning along the same line while varying the current density between ± 0.8 mA μm^{-1} .

The dashed arrows represent positions where the averaged line profiles in **c** were taken. A one-dimensional Fourier filter was applied for **b** only, to reduce visual noise. **c**, Averaged (± 25 $\mu\text{A} \mu\text{m}^{-1}$) SPP line profiles at different current densities. The circles are raw data; the solid lines are fitting results; the dashed line is a guide to the eye. The line profiles are shifted vertically for clarity. **d**, Fitted SPP line profiles without d.c. current (black) and with $J_{dc} = 0.69$ mA μm^{-1} (blue), illustrating a reduction of the SPP wavelength. a.u., arbitrary units.

on the quasiparticle collision rate Γ_{ee} (Supplementary Information). In particular, $\eta = 1/4$ in the kinetic regime where Γ_{ee} is small compared to the measurement frequency $\omega = 890$ $\text{cm}^{-1} = 26.7$ THz. The prediction of equation (1) for the kinetic regime is plotted by the black solid lines in Fig. 3a, b. Provided $\Gamma_{ee} > \omega$ —the regime where graphene quasiparticles behave collectively as a hydrodynamic fluid^{27–29}—the drag coefficient assumes $\eta = 1/2$, which is plotted by blue dashed lines in Fig. 3a, b. Here we ignore, for simplicity, the Fermi liquid interaction effects³⁰. For our

experimental condition, we estimate that $\Gamma_{ee} \sim T^2 / |\hbar v_F \sqrt{n}| < 1$ THz, which strongly suggests that $\eta = 1/4$ should be appropriate, in agreement with the experimental data. It is also instructive to compare these results with previous works (Supplementary Table) on the Fizeau shift (often referred to as the Doppler shift) in plasma^{5,31} and in GaAs semiconductor structures^{6,7,32}. Such systems have parabolic quasiparticle dispersions, which are invariant under a Galilean transformation. However,

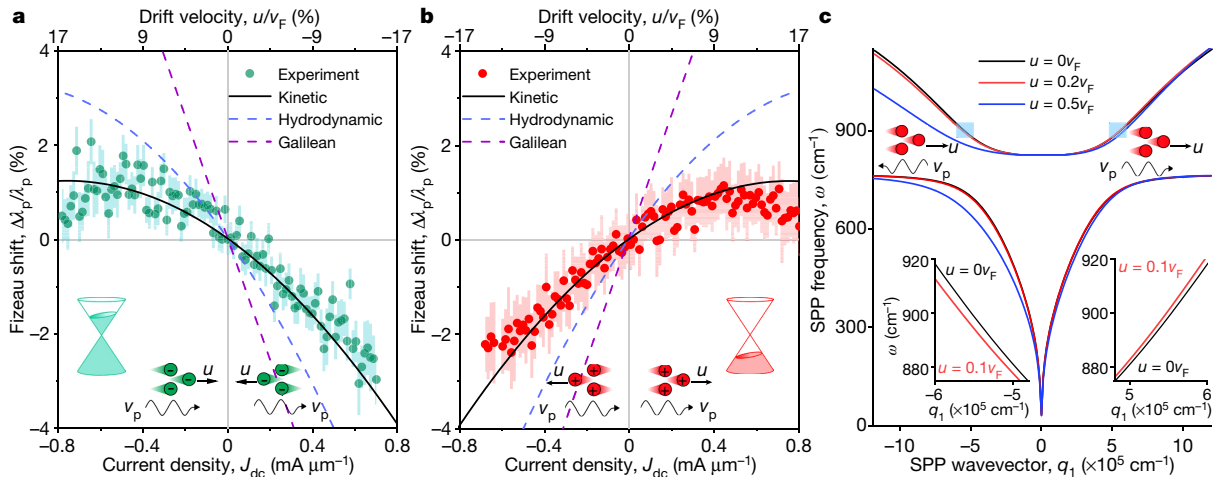


Fig. 3 | Quantitative analysis of the plasmonic Fizeau drag. **a**, The Fizeau shift, $\Delta\lambda_p/\lambda_p$ (circles), extracted from fitted line profiles as a function of current density and carrier drift velocity at $V_g = 47$ V and $T = 170$ K. Error bars represent ± 1 standard deviation of the fitted Fizeau shift. Lines represent theoretical predictions of Fizeau shift for the kinetic regime (black solid line), the hydrodynamic regime

(blue dashed line), and a 2D electron gas with parabolic dispersion (purple dashed line), respectively. **b**, As in **a**, at $V_g = -47$ V and $T = 170$ K. **c**, SPP dispersion at carrier density $n = 2.9 \times 10^{12}$ cm^{-2} calculated for the kinetic regime (Supplementary Information). The gap in the dispersion stems from phonon resonances in the hBN. Insets show enlarged views of the regions marked by the light blue boxes.

graphene quasiparticles are massless Dirac fermions characterized by a quasi-Lorentz invariance, with the speed of light replaced by v_F . As indicated by the purple dashed lines in Fig. 3a, b, the Fizeau shift of plasmons in a Galilean-invariant system depends linearly on the drift velocity, with unit drag coefficient $\eta = 1$. The obvious discrepancy of these predictions with our experimental data vividly demonstrates that the Galilean invariance is broken in graphene.

Additional insights into the Fizeau shift can be obtained by placing our results in the context of the nonlinear electrodynamics of graphene²⁹. The current response at the plasmonic frequency ω can be expanded as $j(\omega) = (\sigma + \sigma^{(2)}E_{dc} + \sigma^{(3)}E_{dc}^2 + \dots)E_{ac}(\omega) \equiv \sigma_{eff}E_{ac}(\omega)$, where $\sigma^{(n)}$ is the n th-order nonlinear optical conductivity component, E_{dc} is the d.c. electric field that drives the static current flow $u \sim E_{dc} + O(E_{dc}^3)$ and $E_{ac}(\omega)$ is the inhomogeneous a.c. field from the launcher. All orders of E_{dc} contribute to the effective a.c. conductivity σ_{eff} , which determines the Fizeau shift. Moreover, the Fizeau shift induced by E_{dc}^k is a signature of $(k+1)$ th-order nonlinearity represented by the component $\sigma^{(k+1)}$. Our data in Fig. 3 show that as the d.c. drive increases, the linear Fizeau shift acquires quadratic corrections: a manifestation of the third-order nonlinearity in $\sigma^{(3)}E_{dc}^2$.

Outlook

The current-induced Fizeau drag of plasmons reveals novel aspects of interactions between infrared photons and Dirac electrons in graphene. Commonly, drag effects are understood as friction-like momentum transfer between two coupled sub-systems. Examples include Coulomb drag between spatially separated conductors^{33,34}, and drag effects between electrons and phonons in a crystal^{35,36}. Our data show that the notion of drag could be extended to the two constituents of a polaritonic quasiparticle: a superposition of infrared photons and Dirac electrons. By ramping up the current in our platform, we solely perturbed the electronic constituent of the quasiparticles. The photonic component reacts by abiding to the rules of quasi-relativistic theory (Supplementary Information). However, the observed effect is not a mere consequence of relativistic kinematics. The plasmonic Fizeau drag in graphene is inherently a non-equilibrium and nonlinear phenomenon the magnitude of which depends on the dynamics of electron–electron, electron–phonon and electron–photon interactions of the Dirac electrons. A task for future experiments is to map the Fizeau drag for the entire SPP dispersion in order to optimize the infrared nonreciprocity for on-chip applications. In principle, plasmonic Fizeau drag offers means to probe the unique motional Fermi liquid effects³⁰ and nonlocal effects³⁷. Fizeau drag experiments can also be extended to double-layer graphene³⁸ and twisted bilayer graphene³⁹, potentially offering intriguing opportunities to probe the physics of Fermi velocity renormalization and strong correlations^{40,41} in electronic systems. Finally, by further enhancing the carrier drift velocity towards the plasmon velocity, Fizeau drag can be boosted, paving the way for plasmonic emission via plasmon instability^{42,43} and amplification^{44–46}.

Online content

Any methods, additional references, Nature Research reporting summaries, source data, extended data, supplementary information, acknowledgements, peer review information; details of author contributions and competing interests; and statements of data and code availability are available at <https://doi.org/10.1038/s41586-021-03640-x>.

1. Fresnel, A., *Théorie de la lumière*. Cinquième section: questions diverses d'optique [Theory of light. Fifth section: various questions of optics]. Letter to F. Arago, September 1818. In *Oeuvres complètes d'Augustin Fresnel* Vol. 2, 627–636 (Imprimerie Impériale, 1868).
2. Fizeau, H. Sur les hypothèses relatives à l'éther lumineux, et sur une expérience qui paraît démontrer que le mouvement des corps change la vitesse avec laquelle la lumière se propage dans leur intérieur [On the relative hypotheses, luminous ether, and on an experiment which seems to demonstrate that the movement of bodies changes the speed with which light propagates in their interior.]. *CR Hebd. Acad. Sci.* **33**, 349–355 (1851).

3. Landau, L. & Lifshitz, E. *The Classical Theory of Fields* Vol. 2 4th edn (Pergamon, 1975).
4. Lorentz, H. A. *The Theory of Electrons and Its Applications to the Phenomena of Light and Radiant Heat* (Teubner, 1916).
5. Unz, H. Relativistic magneto-ionic theory for drifting plasma in longitudinal direction. *Phys. Rev.* **146**, 92–95 (1966).
6. Moss, T., Burrell, G. & Hetherington, A. Measurement of Fresnel drag produced by electron motion in semiconductors. *Proc. Roy. Soc. London Ser. A* **308**, 125–132 (1968).
7. Almazov, L., Vas'ko, F. & Dykman, I. Influence of carrier drift on the propagation of electromagnetic wave in a solid-state plasma. *JETP Lett.* **16**, 241–216 (1972).
8. Basov, D. N., Fogler, M. M. & García de Abajo, F. J. Polaritons in van der Waals materials. *Science* **354**, aag1992 (2016).
9. Low, T. et al. Polaritons in layered two-dimensional materials. *Nat. Mater.* **16**, 182–194 (2017).
10. Caloz, C. et al. Electromagnetic nonreciprocity. *Phys. Rev. Appl.* **10**, 047001 (2018).
11. Jin, D. et al. Infrared topological plasmons in graphene. *Phys. Rev. Lett.* **118**, 245301 (2017).
12. Tokura, Y. & Nagaosa, N. Nonreciprocal responses from non-centrosymmetric quantum materials. *Nat. Commun.* **9**, 3740 (2018).
13. Kumar, A. et al. Chiral plasmon in gapped Dirac systems. *Phys. Rev. B* **93**, 041413 (2016).
14. Song, J. C. W. & Rudner, M. S. Chiral plasmons without magnetic field. *Proc. Natl Acad. Sci. USA* **113**, 4658–4663 (2016).
15. Jablan, M., Buljan, H. & Soljačić, M. Plasmonics in graphene at infrared frequencies. *Phys. Rev. B* **80**, 245435 (2009).
16. Woessner, A. et al. Highly confined low-loss plasmons in graphene–boron nitride heterostructures. *Nat. Mater.* **14**, 421 (2015).
17. Dai, S. et al. Graphene on hexagonal boron nitride as a tunable hyperbolic metamaterial. *Nat. Nanotechnol.* **10**, 682–686 (2015).
18. Ni, G. X. et al. Fundamental limits to graphene plasmonics. *Nature* **557**, 530–533 (2018).
19. Son, S.-K. et al. Graphene hot-electron light bulb: incandescence from hBN-encapsulated graphene in air. *2D Mater.* **5**, 011006 (2017).
20. Borgnia, D. S., Phan, T. V. & Levitov, L. S. Quasi-relativistic Doppler effect and non-reciprocal plasmons in graphene. Preprint at: <https://arxiv.org/abs/1512.09044> (2015).
21. Sabbaghi, M., Lee, H.-W., Stauber, T. & Kim, K. S. Drift-induced modifications to the dynamical polarization of graphene. *Phys. Rev. B* **92**, 195429 (2015).
22. Duppel, B. V., Tomadin, A., Grigorenko, A. N. & Polini, M. Current-induced birefringent absorption and non-reciprocal plasmons in graphene. *2D Mater.* **3**, 015011 (2016).
23. Bliokh, K., Rodríguez-Fortuño, F. J., Bekshaev, A., Kivshar, Y. & Nori, F. Electric-current-induced unidirectional propagation of surface plasmon-polaritons. *Opt. Lett.* **43**, 963–966 (2018).
24. Sabbaghi, M., Lee, H.-W. & Stauber, T. Electro-optics of current-carrying graphene. *Phys. Rev. B* **98**, 075424 (2018).
25. W. Zhao et al. Efficient Fizeau drag from Dirac electrons in monolayer graphene. *Nature* <https://www.nature.com/articles/s41586-021-03574-4> (2021).
26. Yu, Y.-J. et al. Tuning the graphene wave function by electric field effect. *Nano Lett.* **9**, 3430–3434 (2009).
27. Svintsov, D., Vyurkov, V., Ryzhii, V. & Otsuji, T. Hydrodynamic electron transport and nonlinear waves in graphene. *Phys. Rev. B* **88**, 245444 (2013).
28. Lucas, A. & Fong, K. C. Hydrodynamics of electrons in graphene. *J. Phys. Condens. Matter* **30**, 053001 (2018).
29. Sun, Z., Basov, D. N. & Fogler, M. M. Universal linear and nonlinear electrodynamics of a Dirac fluid. *Proc. Natl Acad. Sci. USA* **115**, 3285–3289 (2018).
30. Gao, H., Dong, Z. & Levitov, L. Plasmonic drag in a flowing Fermi liquid. Preprint at <https://arxiv.org/abs/1912.13409> (2020).
31. Brower, D. L. et al. Fizeau interferometer for measurement of plasma electron current. *Rev. Sci. Instrum.* **75**, 3399–3401 (2004).
32. Tyson, R. E. et al. Far-infrared studies of the plasmon resonance of a drifting 2DEG. *Superlattices Microstruct.* **12**, 371–374 (1992).
33. Gramila, T. J., Eisenstein, J. P., MacDonald, A. H., Pfeiffer, L. N. & West, K. W. Mutual friction between parallel two-dimensional electron systems. *Phys. Rev. Lett.* **66**, 1216–1219 (1991).
34. Gorbachev, R. V. et al. Strong Coulomb drag and broken symmetry in double-layer graphene. *Nat. Phys.* **8**, 896–901 (2012).
35. Gurevich, Y. G. & Mashkevich, O. L. The electron–phonon drag and transport phenomena in semiconductors. *Phys. Rep.* **181**, 327–394 (1989).
36. Narozhny, B. N. & Levchenko, A. Coulomb drag. *Rev. Mod. Phys.* **88**, 025003 (2016).
37. Lundberg, M. B. et al. Tuning quantum nonlocal effects in graphene plasmonics. *Science* **357**, 187–191 (2017).
38. Morgado, T. A. & Silveirinha, M. G. Nonlocal effects and enhanced nonreciprocity in current-driven graphene systems. *Phys. Rev. B* **102**, 075102 (2020).
39. Papaj, M. & Lewandowski, C. Plasmonic nonreciprocity driven by band hybridization in moiré materials. *Phys. Rev. Lett.* **125**, 066801 (2020).
40. Bistritzer, R. & MacDonald, A. H. Moiré bands in twisted double-layer graphene. *Proc. Natl Acad. Sci. USA* **108**, 12233–12237 (2011).
41. Cao, Y. et al. Correlated insulator behaviour at half-filling in magic-angle graphene superlattices. *Nature* **556**, 80–84 (2018).
42. Dyakonov, M. & Shur, M. Shallow water analogy for a ballistic field effect transistor: new mechanism of plasma wave generation by dc current. *Phys. Rev. Lett.* **71**, 2465–2468 (1993).
43. Gupta, R. & Ridley, B. Two-stream instability in two-dimensional degenerate systems. *Phys. Rev. B* **39**, 6208 (1989).
44. Aizin, G. R., Mikalopas, J. & Shur, M. Current-driven plasmonic boom instability in three-dimensional gated periodic ballistic nanostructures. *Phys. Rev. B* **93**, 195315 (2016).
45. Zolotovskii, I. O. et al. Plasmon-polariton distributed-feedback laser pumped by a fast drift current in graphene. *Phys. Rev. A* **97**, 053828 (2018).
46. Smetanin, I. V., Bouhelier, A. & Uskov, A. V. Coherent surface plasmon amplification through the dissipative instability of 2D direct current. *Nanophotonics* **8**, 135–143 (2018).

Publisher's note Springer Nature remains neutral with regard to jurisdictional claims in published maps and institutional affiliations.

© The Author(s), under exclusive licence to Springer Nature Limited 2021

Methods

Device fabrication

Our devices involve monolayer graphene⁴⁷ encapsulated in monoisotopic hexagonal boron nitride crystals⁴⁸ ($h^{11}\text{BN}$) with a global silicon gate, fabricated using a dry transfer technique^{49–51}. We first mechanically exfoliated graphene and hBN on an oxidized Si wafer, and searched for sizable, uniform flakes using optical contrast. Using a homemade transfer system, we picked up a thin (<10 nm) crystal of hBN as well as a thicker (>20 nm) neighbouring crystal with a polycarbonate (PC) membrane suspended over a thick (4 mm) polydimethylsiloxane (PDMS) polymer block mounted on a micromanipulator and heated to 100 °C. The thicker neighbouring flake was used as a marker to determine the position of the thin hBN, which, once on the PC, has extremely low optical contrast. The thin hBN was then used to pick up a monolayer graphene flake at room temperature. Finally, the two-layer stack was transferred onto the thick (>50 nm) hBN flake at elevated temperatures (160–170 °C)—a technique that we found resulted in clean, hydrocarbon-free van der Waals interfaces⁵⁰. We inspected the final heterostructure using atomic force microscopy (AFM) and selected flat, wrinkle-free areas for our device.

The heterostructures were covered by a polymethyl-methacrylate (PMMA) resist, and electron-beam lithography was used to define a protective mask in the shape of the device. We selectively etched away the exposed parts of the heterostructure with reactive ion etching (RIE) using plasma generated by Ar, CHF_3 and O_2 gases. We then performed a second round of electron-beam lithography and etching to define contact areas. These areas were first processed by a mild O_2 plasma to remove PMMA residuals. We then performed RIE using a combination of O_2 and CHF_3 gases to selectively etch away the top hBN only. 3 nm chromium and 50–70 nm gold were deposited into the etched regions via thermal evaporation at high vacuum (10^{-7} mbar). The combination of the selective etching recipe and the high vacuum thermal evaporation ensured low-resistance contacts crucial for our high-current experiments⁵². Gate voltages reported in this manuscript are measured from the charge neutrality point.

The monoisotopic hexagonal boron nitride ($h^{11}\text{BN}$) crystals were synthesized by metal flux method at atmospheric pressure. The starting materials, Ni (99.999%), Cr (99.999%) and ^{11}B (>99 at%) powders mixed in a 12:12:1 weight ratio, were loaded into an alumina crucible which was then placed into a single-zone tube furnace. The powder mixture was heated to 1,550 °C by 24 h and held for 48 h under N_2/H_2 : 100/1 standard cubic centimetres per minute (sccm) with 840 torr chamber pressure. Afterwards, it was slowly cooled down to 1,525 °C at a rate of 0.5 °C h^{-1} and quickly quenched to room temperature. The $h^{11}\text{BN}$ crystals formed onto the metal surface were subsequently peeled off by scotch tape.

Cryogenic scanning near-field imaging

Cryogenic near-field imaging was performed using a home-built scattering-type scanning near-field optical microscope operating at low temperature and ultrahigh vacuum based on Attocube scanner. We used a tapping-mode AFM operating at a frequency of ~275 kHz. A mid-infrared continuous-wave CO_2 laser (Access Laser) was focused on the sample, exciting the gold bar to launch propagating SPPs. The scattered light was collected by an off-axis parabolic mirror and recorded with a HgCdTe (MCT) detector. Using the pseudo-heterodyne interferometric method⁵³, we extracted the near-field signal at the third harmonic of the tip tapping frequency to suppress the background contribution. AFM topography is registered simultaneously with the near-field data. Data are collected at multiple lines in the middle of device where polaritons propagate with minimal extrinsic distortions.

Current and voltage appliance

We use one source meter (Keithley 2450) to source d.c. current through the whole device while maintaining the gate voltage using another

source meter (Keithley 2450). The d.c. transport of the device is measured by a lock-in amplifier (SR 830) and the current-induced potential change at the gold launcher is monitored by a multimeter (Keithley DMM 6500).

Gate-dependent transport

Low contact resistance enables the application of high electric current through a graphene device and promotes an appreciable plasmonic Fizeau effect. We measured the contact resistance of a typical device using the two-terminal resistance method (Extended Data Fig. 1). As schematically shown in the inset of Extended Data Fig. 1, we sourced 100 nA of current through the graphene channel and measured the voltage drop across the entire device. The gate voltage dependence of the two-terminal resistance $R_{2\text{pt}}$ shows a typical bell-shaped curve with a charge neutrality point at $V_g = -7.5$ V. At high gate voltage $|V_g| > 40$ V where we acquired our Fizeau drag data, $R_{2\text{pt}}$ is only 200–300 Ω . Considering that the sheet resistivity ρ of high-quality graphene devices at high gate voltage⁵⁴ is of the order of 50 Ω , the total sheet resistance of our entire device is around 150 Ω . This suggests that the typical graphene–metal interface in our device has a resistance of less than 100 Ω . The ultra-low contact resistance enables us to drive a large current through the graphene channel using a small bias voltage, thereby mitigating the current-gating effects described in Methods section ‘Current-gating effect’.

Current-gating effect

The current-gating effect manifests itself as changes in the local carrier density caused by the spatial variation of the electrostatic potential in the graphene, owing to the biasing current. An appreciable current-gating effect is expected when high source/drain voltage is applied across the graphene. Since the SPP wavelength is sensitive to the local carrier density, it is imperative to evaluate the role of the current-gating effect in our Fizeau drag experiment.

To examine the magnitude of the current-gating effect, we measured the electrostatic potential of the launcher while sourcing large current (Extended Data Figs. 2, 3). Because the electrostatic potential close to the drain electrode changes minimally as a function of current, the current-gating effect is minimized close to the drain where we performed all of our plasmonic imaging experiments (Extended Data Fig. 2). Voltages on both the source electrode and the SPP launcher are recorded at the same time (Extended Data Fig. 3). The voltage on the SPP launcher depends linearly on the applied current with slope 150 mV/(mA μm^{-1}), whereas the total two-terminal voltage reveals non-linear behaviour. Standard graphene SPP dispersion implies that $\lambda_p \propto \sqrt{V_g}$. We estimate the plasmon wavelength shift caused by the current-gating effect to be

$$\frac{\Delta\lambda_p}{\lambda_p} = \frac{1}{2} \frac{\Delta V_g}{V_g} = \frac{1}{2} \frac{0.15 \text{ V}/(\text{mA } \mu\text{m}^{-1})}{50 \text{ V}} = 0.15\% / (\text{mA } \mu\text{m}^{-1}). \quad (2)$$

Thus, the change in the SPP wavelength induced by the current-gating effect is much smaller than the 2% Fizeau effect observed in our measurements.

Large-area near-field images

In a typical near-field experiment, AFM topography and near-field images are registered simultaneously. Extended Data Fig. 4 shows representative near-field and AFM images without current at $T = 170$ K and $V_g = 50$ V. Near the graphene edge, we observed $\lambda_p/2$ -periodic fringes (top and bottom areas of the field of view in Extended Data Fig. 4a as well as Extended Data Fig. 4c, d). These characteristic $\lambda_p/2$ -periodic fringes are plasmonic waves excited by the near-field probe and reflected by the graphene edge. The $\lambda_p/2$ plasmons complete a ‘round trip’ and are subsequently out-coupled by the near-field probe. In contrast, SPPs close to the gold (left region of the field of view in Extended Data

Article

Fig. 4a) are excited by the gold launcher and propagate to the right. The periodicity of Au-launched plasmon fringes equals the SPP wavelength λ_p . In our Fizeau drag experiment, we focused on the λ_p fringe excited by the gold launcher.

Data in Extended Data Fig. 4 attest that our device is free from cracks, wrinkles, bubbles and folds, as can be seen from our near-field images (Extended Data Fig. 4a). To minimize the role of these extrinsic factors in Fizeau drag experiment, we scanned along the exact same line in real space for each set of data. These extrinsic factors are not affected by current biasing and thus cannot contribute to the changes in SPP wavelength observed in the Fizeau drag experiment.

Besides the Fizeau effect of gold-launched plasmons studied in the current work, edge-reflected $\lambda_p/2$ plasmons (Extended Data Fig. 4) could reveal higher-order Fizeau effects. Furthermore, current flow near the edges of graphene may be considerably different than its counterpart in the interior of graphene. These intriguing phenomena are beyond the scope of the current study and could motivate future explorations of the intricate interplay between the current flow and plasmon standing waves near graphene edges.

Possible extrinsic factor: Joule heating

The d.c. current could heat up the electronic system to $T' = T[1 + C_t(u^2/v_F^2)]$, where T is the lattice temperature and C_t is some constant. This effect primarily decreases the plasmon lifetime, but can also affect the plasmon wavelength. The Drude weight of graphene is known to be slightly temperature-dependent²⁹, $D(n, T) \approx D(n, 0)[1 - (\pi^2/6)(T/\mu_0)^2]$ at $T \ll \mu_0$, where μ_0 is the Fermi energy. Hence, the Joule heating leads to a reduction of plasmon wavelength by the relative amount

$$\frac{\Delta\lambda_p}{\lambda_p} = \frac{D(n, T')}{D(n, T)} - 1 \approx \frac{1 - \frac{\pi^2}{6}\left(\frac{T'}{\mu_0}\right)^2}{1 - \frac{\pi^2}{6}\left(\frac{T}{\mu_0}\right)^2} - 1 \quad (3)$$

$$\approx -\frac{\pi^2}{6} \frac{T^2}{\mu_0^2} \left(\frac{2C_t u^2}{v_F^2} + \frac{C_t^2 u^4}{v_F^4} \right).$$

For a rough estimate, we take $T = 170$ K and $T' = 200$ K at the experimentally accessible drift velocity $u = 0.17v_F$, which implies $C_t \approx 6$. The corresponding plasmon wavelength shift is $\Delta\lambda_p/\lambda_p = -0.35\%$. Such a heating effect may explain the small discrepancy between the measurements and the theoretical predictions of the Fizeau shift at the largest current in Fig. 3.

Absence of mechanical distortion

As described in the main text, we carried out near-field scans along the same line in the middle of the graphene channel (dark red region in Fig. 2a) while continuously changing the current. At different current densities, the topographic line profiles repeat themselves (Extended Data Fig. 5b), whereas the near-field line profiles clearly show a Fizeau shift (Extended Data Fig. 5d). These findings unequivocally support that our measurements are free from mechanical distortions and that the extracted Fizeau shift is reliable.

Fitting method

We used a damped sinusoidal function with far-field background

$$y = A \sin(q_x x - B) \exp(-q_z x) + Cx + D, \quad (4)$$

to model the line profiles of the near-field signals of propagating SPPs, where $\beta = \{A, B, C, D, q_1, q_2\}$ is the set of fitting parameters and the SPP wavelength is $\lambda_p = 2\pi/q_1$. To estimate the parameters β of the nonlinear model, we minimized the chi-squared value:

$$\chi^2 = \sum_i \frac{(y_{\text{exp},i} - y_i(\beta))^2}{\sigma_y^2}, \quad (5)$$

where $y_{\text{exp},i}$ and $y_i(\beta)$ are experimental and model-predicted signals, respectively, and σ_y^2 is the signal variance. We minimized χ^2 using the Levenberg–Marquardt algorithm (LMA) and set the convergence criteria of LMA as $\Delta\chi^2/\chi^2 < 10^{-4}$. The reduced chi-squared value used to quantify the goodness of fit equals $\chi^2/60 \approx 1$, indicating a good fit. The denominator in the definition of the reduced chi-squared value is the number of pixels in a line profile minus the number of fitting parameters.

If the β are Gaussian random variables, the covariance matrix is inversely proportional to the Hessian matrix $\nabla^2 \chi^2(\beta)$, which is approximated to first order by the matrix product of Jacobians J evaluated at the best-fit values of the parameters:

$$\Sigma = \sigma_y^2 (J^T J)^{-1}; \quad J_{ij} = \frac{\partial y_i}{\partial \beta_j}. \quad (6)$$

The standard deviations of the fitted wavelengths σ_λ are the square roots of the corresponding diagonal terms in the covariance matrices of the various line profiles. We typically extract $\sigma_\lambda < 1$ nm for our experiments, which corresponds to $< 0.8\%$ relative error for the fitted SPP wavelength. The error bars presented in Fig. 3 are 68% confidence intervals computed from σ_λ . Alternative estimates of confidence intervals using likelihood-based methods give similar results. The likelihood-based estimates include all wavelength estimates with χ^2 value smaller than $\chi_{\text{best fit}}^2 + \chi^2(0.68, 6)$, where $\chi^2(0.68, \text{df})$ is the 68% quantile of a chi-squared distribution with df degrees of freedom⁵⁵. The maximum correlation between the wavelength and any other fitting parameter (A, B, C, D, q_2) is 3.5%. This means that the additional fitting parameters have little effect on the optimal value and the variance of the extracted wavelength.

Monte Carlo simulation of regression coefficients

Here we justify the above-mentioned empirical estimates of σ_λ with Monte Carlo simulations. Supposing there are experimental imperfections from signal noise, pixel size, and limited spatial resolution in a near-field measurement, then the empirical standard deviation of the wavelength $\sigma_\lambda < 1$ nm may seem unrealistic. However, SPP line profiles observed in the experiments have up to six periods. The ‘redundant’ information in a periodic function enhances the precision of parameter estimates beyond the limited pixel size and spatial resolution of the near-field technique to support a statistically significant Fizeau shift. We demonstrate this by computing the variance σ_λ and bias $\mathbb{E}[\hat{\lambda}] - \lambda_p$ of the least-squares wavelength estimate numerically for simulated line profiles that take into account all experimental imperfections, such as additive signal noise, positioner noise, limited spatial resolution and pixel size.

Consider equation (4) in the presence of noise and limited spatial resolution:

$$\tilde{y} = G(x, \text{SR})[A \sin(q_x x - B) \exp(-q_z x) + Cx + D] + \varepsilon, \quad (7)$$

where the limited positioning precision adds uncertainty to the spatial position σ_x such that the total noise ε is heteroscedastic and satisfies a normal distribution with an effective variance⁵⁵ $\sigma_y^2 + \left(\sigma_x \frac{\partial y}{\partial x}\right)^2$, $\varepsilon \sim \mathcal{N}(0, \sigma_y^2 + \left(\sigma_x \frac{\partial y}{\partial x}\right)^2)$, where \sim indicates ‘is distributed as’ and $\mathcal{N}(\mu, \sigma^2)$ is the normal distribution with mean μ and variance σ^2 . We model the limited spatial resolution (SR) in a near-field experiment by a Gaussian filter, that is, convolution with a Gaussian function $G(x)$ with a full-width at half-maximum given by SR. This has the effect of blurring sharp edges and peaks in the near-field signal. The spatial resolution of a near-field measurement is limited by the spatial extent of evanescent fields under the tip apex. The evanescent field averages the sample response weighted by distance from the tip apex in a qualitatively Gaussian fashion⁵⁶.

In Extended Data Fig. 6a, we show the distribution of wavelengths estimated by solving equation (5) with LMA in a Monte Carlo simulation

of $N = 10,000$ random replications of equation (7) with $SR = 20$ nm, $\sigma_y/A = 10\%$, and $\sigma_x = 1$ nm (determined from scanner specifications). The true parameters in the simulations were $\lambda_p = 2\pi/q_1 = 118$ nm, $1/q_2 = 2.75\lambda_p$, $A = 1$, and $B = C = D = 0$. A few representative line profiles are shown in Extended Data Fig. 6b. These simulation parameters are extracted from typical experimental conditions. The distribution of the fitted wavelength is Gaussian (p value from Jarque–Bera test, <0.01) with a standard deviation $\sigma_\lambda = 0.71$ nm < 1 nm, consistent with the empirical estimates from the covariance matrices.

We carefully studied the relationship between the error of the SPP wavelength estimate and various experimental conditions (Extended Data Fig. 6c, d). We can decompose the mean-squared error of the SPP wavelength estimate into bias (blue coloured lines in Extended Data Fig. 6c, d) and variance (red coloured lines in Extended Data Fig. 6c, d). We notice that the variance of the wavelength estimate is minimally affected by spatial resolution (Extended Data Fig. 6c.I) and pixel size (Extended Data Fig. 6c.II) under realistic experimental conditions. Limited spatial resolution will bias the wavelength estimate and the bias grows with the degradation of spatial resolution (blue line in Extended Data Fig. 6c.I). However, as long as $SR < 30$ nm, the bias and variance will be smaller than 1 nm. Since the spatial resolution is deterministic in this model, it alone cannot degrade the precision of the wavelength estimate. However, it does couple to random noise to increase the variance of the wavelength estimate (the Gaussian filter reduces f''), as shown by the dark red line in Extended Data Fig. 6c.I. The pixel size of the line profiles has a vanishingly small effect on the wavelength estimate as long as the sampling is done well above the Nyquist rate set by the wavelength (Extended Data Fig. 6c.II).

We noticed that the variance of the wavelength estimate is strongly affected by the experimental signal noise (Extended Data Fig. 6d.I) and SPP propagation length (Extended Data Fig. 6d.II). The green curve in Extended Data Fig. 6d.I shows that with unlimited spatial resolution ($SR = 0$) and $\sigma_x = 0$, the dependence of σ_λ on σ_y has the linear form that is given by equation (6) for signal noise levels below 25%. At or above 25% noise, the LMA is unreliable, converging to many outliers such that the wavelength distribution is non-normal. As long as $\sigma_y/A < 10\%$ with $1/q_2 = 2.75\lambda_p$, the estimated $\sigma_\lambda < 1$ nm. In Extended Data Fig. 6d.II, both the variance and the bias of the wavelength estimate decrease with the increase of $1/q_2$. If we only observed a few SPP fringes with short propagation length, the error of our wavelength estimates would be much higher, approaching the limit set by the spatial resolution of the near-field technique.

In conclusion, our rigorous Monte Carlo simulation is consistent with the empirical analysis for the standard deviation of the wavelength estimate σ_λ . Even though we are limited to ~ 20 nm spatial resolution and ~ 10 nm pixel size, as long as the signal noise σ_y is small and the SPP propagation length $1/q_2$ is large, we can extract very accurate ($\sigma_\lambda < 1$ nm) wavelength estimates by fitting line profiles consisting of multiple SPP fringes.

Hypothesis testing on the existence of Fizeau shift

In Extended Data Fig. 6e, we set up a statistical hypothesis test based on the data in Fig. 3 to determine if we can reject a trivial model where there is no Fizeau shift. Consider a linear regression model for the Fizeau shift in a form reminiscent of equation (1):

$$y = X\beta + \varepsilon, \quad (8)$$

$$y_k = (\Delta\lambda_p)_k = \beta_0 + \beta_1 \frac{u_k}{v_{F,k}} + \beta_2 \left(\frac{u_k}{v_{F,k}} \right)^2, \quad (9)$$

where the measurement error $\varepsilon_k \sim \mathcal{N}(0, \sigma_{\Delta\lambda}^2)$. Fitting to the data in Fig. 3a, b, we can obtain a least-square estimate of the coefficients $\hat{\beta} = [-0.42 \ 12.31 \ -72.16]$. A linear hypothesis can be formulated by a set of N restrictions on the linear regression model. The restrictions are generally

$$R\beta = q, \quad (10)$$

and the null (H_0) and alternative (H_1) hypotheses implied by the restrictions are as follows:

$$H_0: R\beta - q = 0, \quad (11)$$

$$H_1: R\beta - q \neq 0. \quad (12)$$

Given the least-squares estimate of the coefficients $\hat{\beta}$, we can estimate the residual vector $R\hat{\beta} - q$. The question of statistical significance boils down to whether the deviation of $R\hat{\beta} - q$ from 0 can be explained by the sampling variability or whether it is significant. We can base a test of H_0 on the Wald statistic, which is chi-squared distributed with N degrees of freedom⁵⁵:

$$W = (R\hat{\beta} - q)^T \{ [R(X^T X)^{-1} R^T]^{-1} (R\hat{\beta} - q) \}^{-1} (R\hat{\beta} - q) = \frac{1}{\sigma_{\Delta\lambda}^2} (R\hat{\beta} - q)^T [R(X^T X)^{-1} R^T]^{-1} (R\hat{\beta} - q). \quad (13)$$

It is usually preferable to use the sample variance $s_{\Delta\lambda}^2$, an estimate of $\sigma_{\Delta\lambda}^2$ with n observations and p parameters. In this case, the F statistic is used instead of the Wald statistic:

$$F = \frac{W}{N} \frac{\sigma_{\Delta\lambda}^2}{s_{\Delta\lambda}^2} = \frac{1}{N s_{\Delta\lambda}^2} (R\hat{\beta} - q)^T [R(X^T X)^{-1} R^T]^{-1} (R\hat{\beta} - q) \approx \frac{\chi^2[N]/N}{\chi^2[n-p]/(n-p)} \equiv F[N, n-p]. \quad (14)$$

For example, in the case of a no-Fizeau-shift model, we would have the following $N = 3$ restrictions:

$$\beta_0 = \alpha, \beta_1 = 0, \beta_2 = 0, \quad (15)$$

which can be expressed as

$$R = \begin{bmatrix} 1 & 0 & 0 \\ 0 & 1 & 0 \\ 0 & 0 & 1 \end{bmatrix}, q = \begin{bmatrix} \alpha \\ 0 \\ 0 \end{bmatrix}. \quad (16)$$

$\Pr(F[3, 217] \leq 2.65) = 0.95$, so we can reject the null hypothesis that this trivial model is supported by the data with 95% confidence if $F > 2.65$. If the trivial model is rejected, then the Fizeau shift is statistically significant since we cannot attribute the current dependence to random noise.

We plot F as a function of $s_{\Delta\lambda}$ in Extended Data Fig. 6e. The standard deviation of the Fizeau shift estimated empirically from the data in Fig. 3 gives $\hat{s} = \sqrt{\frac{1}{n-p} [y - X\hat{\beta}]^2} = 0.74$ nm, which is consistent with the standard deviation from the covariance matrix of experimental line profiles in Methods section ‘Fitting method’ and with the Monte Carlo simulation in Methods section ‘Monte Carlo simulation of regression coefficients’. With this sample standard deviation and $\alpha = 0$, we compute an F statistic for the trivial model of $260.3 > 2.65$ (purple solid line in Extended Data Fig. 6e). We can similarly entertain a model with no current dependence but a constant shift such that $\alpha = \mathbb{E}[\Delta\lambda_p] = -0.78$ nm. This test yields $F = 159.8 > 2.65$ (red solid line in Extended Data Fig. 6e). Statistical hypothesis testing thus suggests that the data are inconsistent to a high degree of certainty with a model that assumes that the data are randomly organized about a constant value (no dependence of the plasmon wavelength shift on the drift velocity). Thus, our experimental data support the existence of a significant Fizeau shift, under the estimated uncertainty.

Data availability

The data that support the findings of this study are available from the corresponding author upon reasonable request.

Code availability

The code used to analyse data are available from the corresponding author upon reasonable request.

47. Zhang, Y., Small, J. P., Pontius, W. V. & Kim, P. Fabrication and electric-field-dependent transport measurements of mesoscopic graphite devices. *Appl. Phys. Lett.* **86**, 073104 (2005).
48. Liu, S. et al. Single crystal growth of millimeter-sized monoisotopic hexagonal boron nitride. *Chem. Mater.* **30**, 6222–6225 (2018).
49. Dean, C. R. et al. Boron nitride substrates for high-quality graphene electronics. *Nat. Nanotechnol.* **5**, 722–726 (2010).
50. Purdie, D. G. et al. Cleaning interfaces in layered materials heterostructures. *Nat. Commun.* **9**, 5387 (2018).
51. Wang, L. et al. One-dimensional electrical contact to a two-dimensional material. *Science* **342**, 614–617 (2013).
52. Ben Shalom, M. et al. Quantum oscillations of the critical current and high-field superconducting proximity in ballistic graphene. *Nat. Phys.* **12**, 318–322 (2016).
53. Ocelic, N., Huber, A. & Hillenbrand, R. Pseudoheterodyne detection for background-free near-field spectroscopy. *Appl. Phys. Lett.* **89**, 101124 (2006).
54. Krishna Kumar, R. et al. Superballistic flow of viscous electron fluid through graphene constrictions. *Nat. Phys.* **13**, 1182 (2017).
55. Meeker, W. Q. & Escobar, L. A. Teaching about approximate confidence regions based on maximum likelihood estimation. *Am. Stat.* **49**, 48–53 (1995).
56. Jiang, B.-Y., Zhang, L. M., Castro Neto, A. H., Basov, D. N. & Fogler, M. M. Generalized spectral method for near-field optical microscopy. *J. Appl. Phys.* **119**, 054305 (2016).

Acknowledgements Research on the physics and imaging of the plasmonic Fizeau effect at Columbia was supported by the US Department of Energy (DOE), Office of Science, Basic

Energy Sciences (BES), under award no. DE-SC0018426. D.A.B. acknowledges the support from MIT Pappalardo Fellowship. M.M.F. is supported by the Office of Naval Research under grant ONR-N000014-18-1-2722. Work in the P.J.-H. group was supported by AFOSR grant FA9550-16-1-0382, the Gordon and Betty Moore Foundation's EPIQS Initiative through grant GBMF9643, and Fundacion Ramon Areces. The development of new nanofabrication and characterization techniques enabling this work has been supported by the US DOE Office of Science, BES, under award DE-SC0019300. The development of the universal cryogenic platform used for scanning probe measurements is supported as part of the Energy Frontier Research Center on Programmable Quantum Materials funded by the US Department of Energy (DOE), Office of Science, Basic Energy Sciences (BES), under award no. DE-SC0019443. The development of infrared nano-optics is supported by Vannevar Bush Faculty Fellowship to D.N.B., ONR-VB: N00014-19-1-2630. D.N.B. is Moore Investigator in Quantum Materials EPIQS #9455. This work also made use of the Materials Research Science and Engineering Center Shared Experimental Facilities supported by the National Science Foundation (NSF) (grant no. DMR-0819762). Support from the Materials Engineering and Processing programme of the National Science Foundation, award number CMMI 1538127 for hBN crystal growth is also greatly appreciated.

Author contributions D.A.B. and D.N.B. conceived and supervised the project. Y.D., L.X., S.Z., D.A.B. and D.N.B. designed the experiments. I.Y.P. and D.A.B. fabricated the devices. S.L. and J.H.E. provided the isotopic hBN crystals. Y.D., L.X., A.S.M. and R.P. performed the experimental measurements. Y.D., L.X., R.J., F.L.R., D.A.B. and D.N.B. analysed the experimental data. Z.S., M.M.F., A.J.M. and L.S.L. developed the theoretical analysis of the experimental data with input from P.J.-H., H.G. and Z.D. Y.D., L.X., Z.S., M.M.F., D.A.B. and D.N.B. co-wrote the manuscript with input from all co-authors.

Competing interests The authors declare no competing interests.

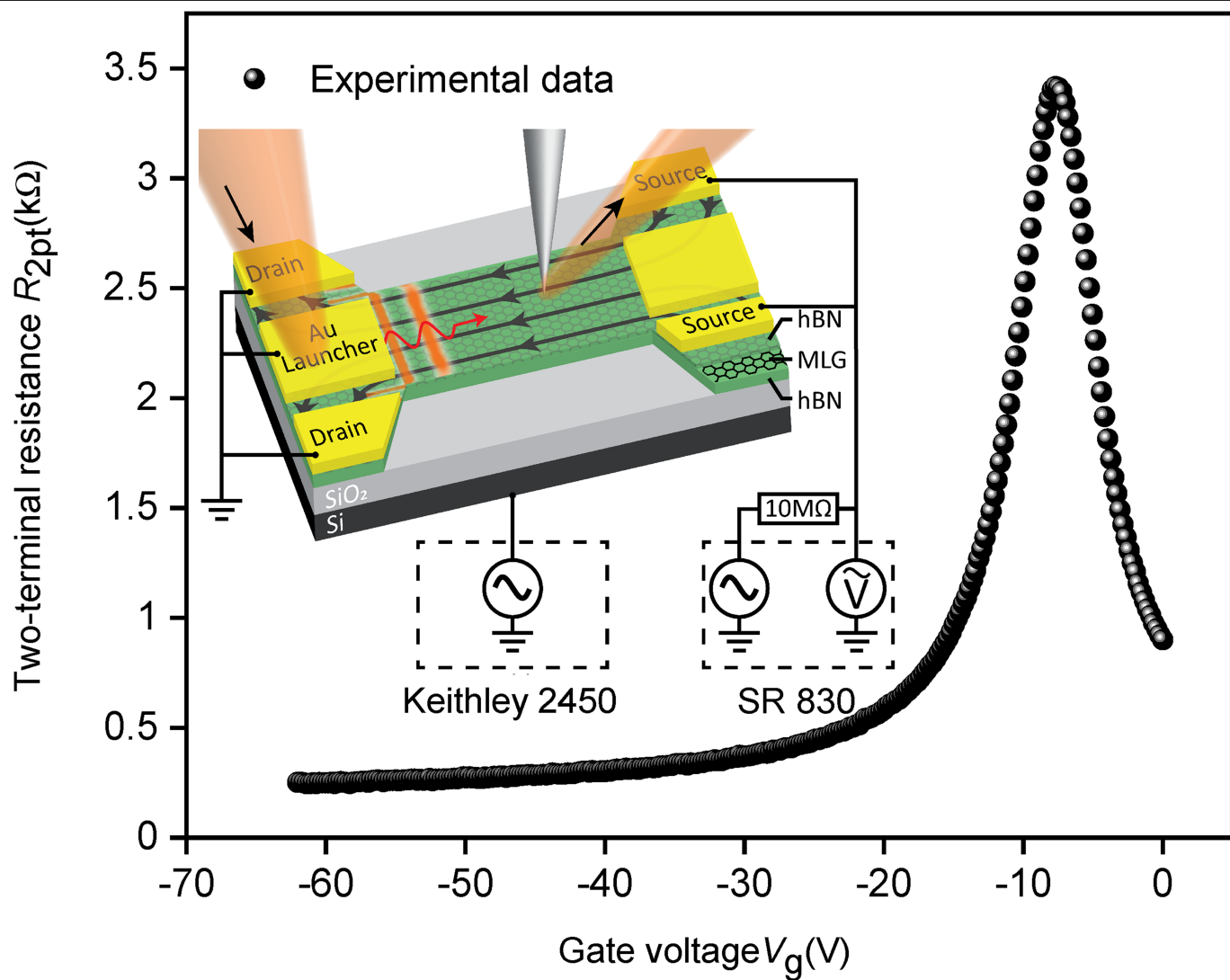
Additional information

Supplementary information The online version contains supplementary material available at <https://doi.org/10.1038/s41586-021-03640-x>.

Correspondence and requests for materials should be addressed to D.A.B. or D.N.B.

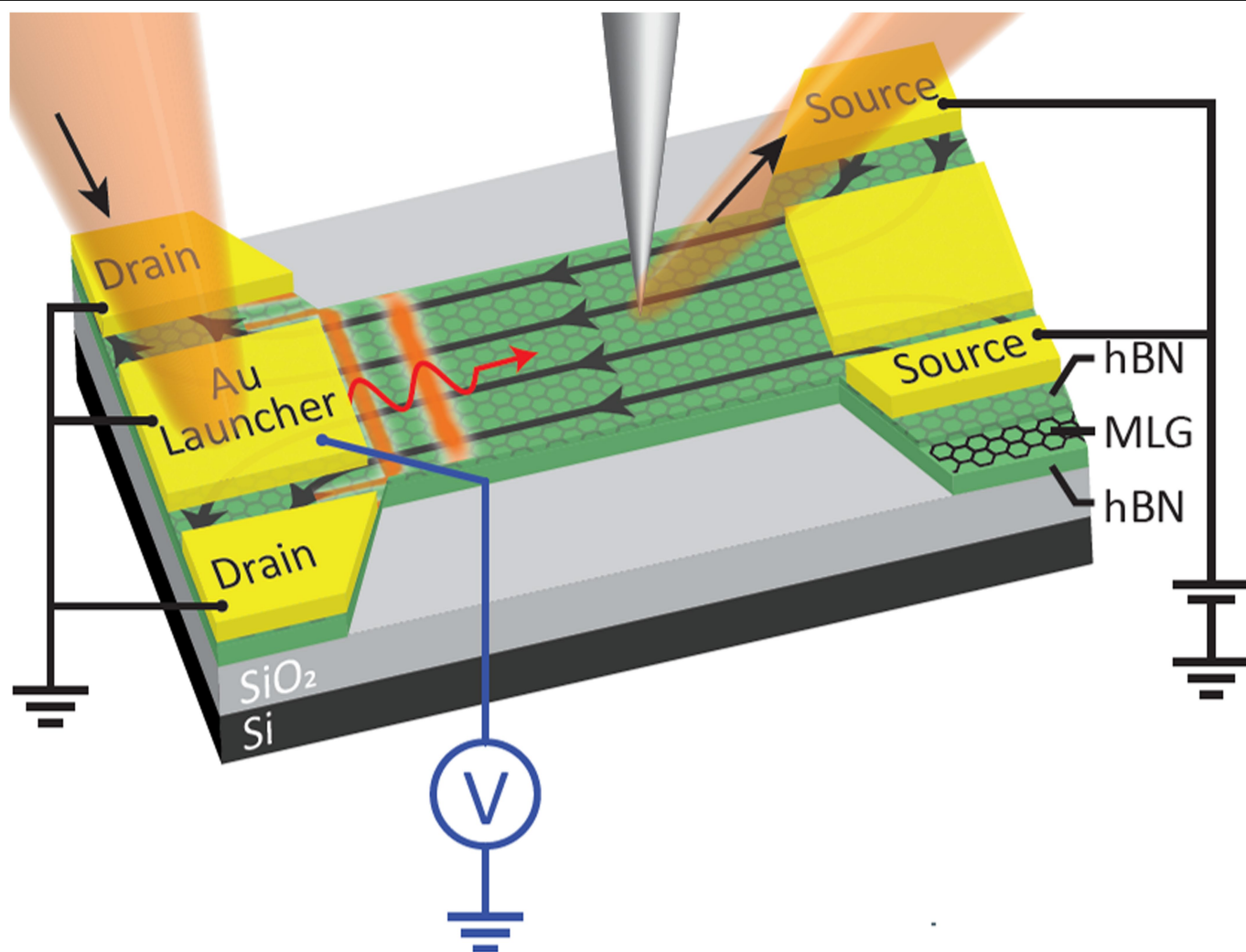
Peer review information *Nature* thanks Joel Cox, Jiahua Duan and Hugen Yan for their contribution to the peer review of this work.

Reprints and permissions information is available at <http://www.nature.com/reprints>.



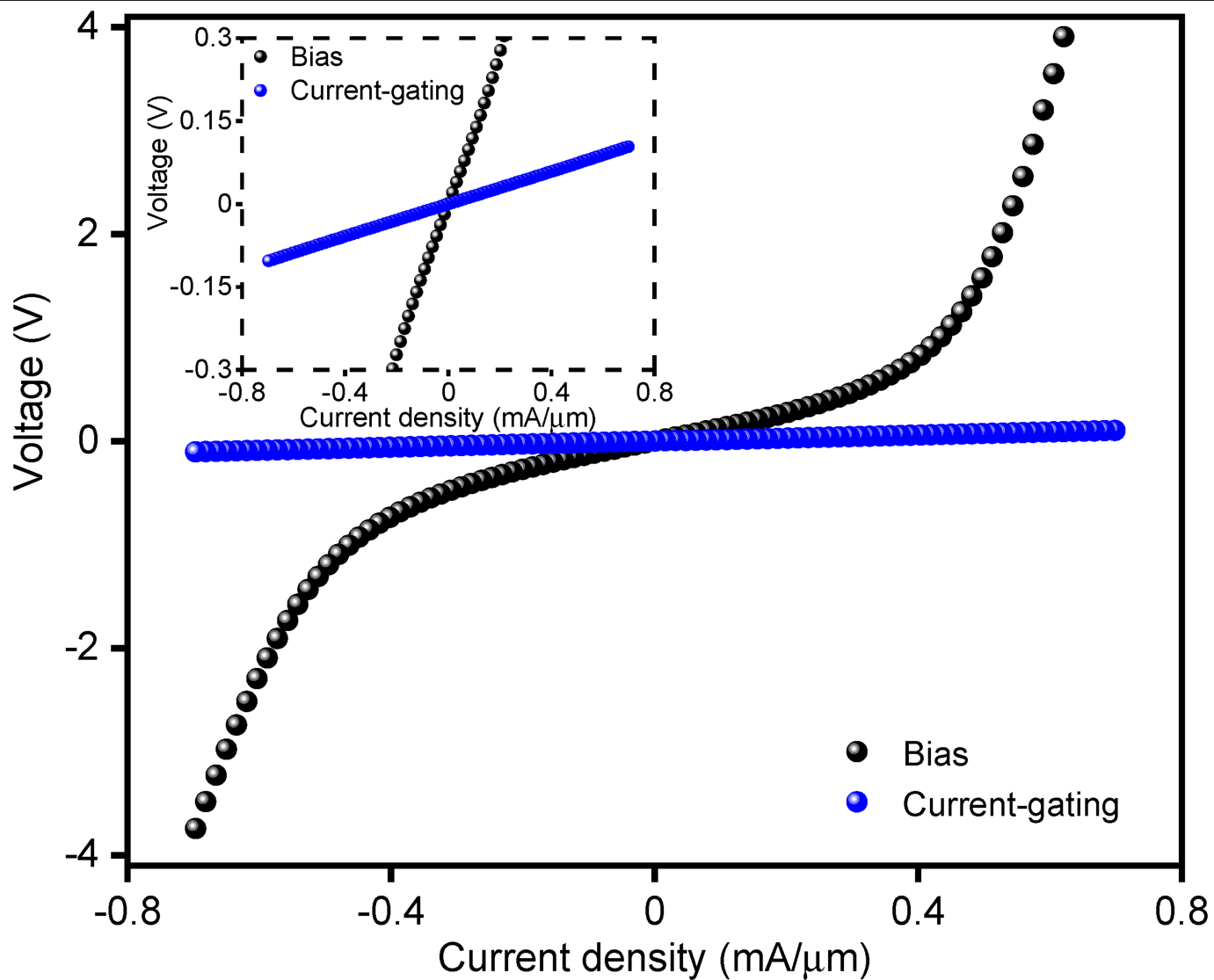
Extended Data Fig. 1 | Gate-dependent transport of a typical device. Two-terminal resistance R_{2pt} of a typical device as a function of the back-gate voltage V_g at $T = 170$ K. Inset shows the transport measurement configuration,

where a source meter (Keithley 2450) was used to source gate voltage, and a lock-in amplifier (SR 830) was used to measure the resistance of the entire device.



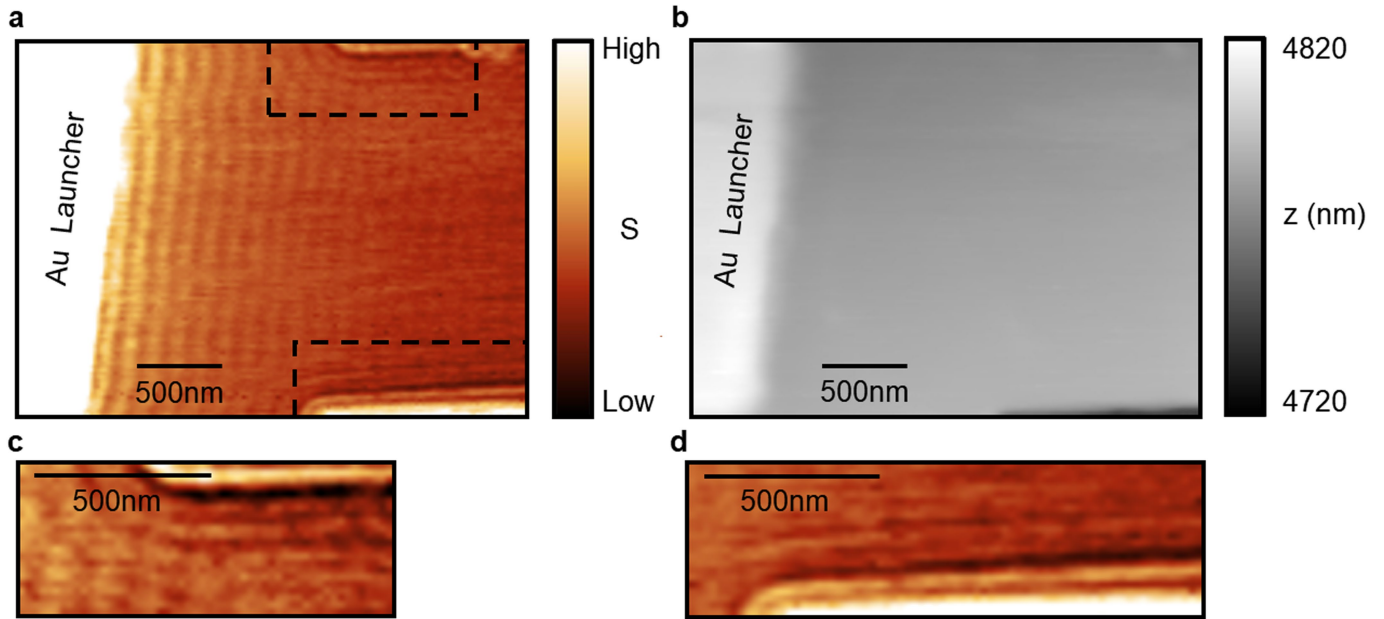
Extended Data Fig. 2 | Experimental configuration for measuring current-gating effects. Voltage is applied across the source/drain electrode and SPP imaging is performed close to the drain. The black streamlines

symbolize the d.c. current. The voltmeter measures the electrostatic potential of the SPP launcher as a function of the biasing current.



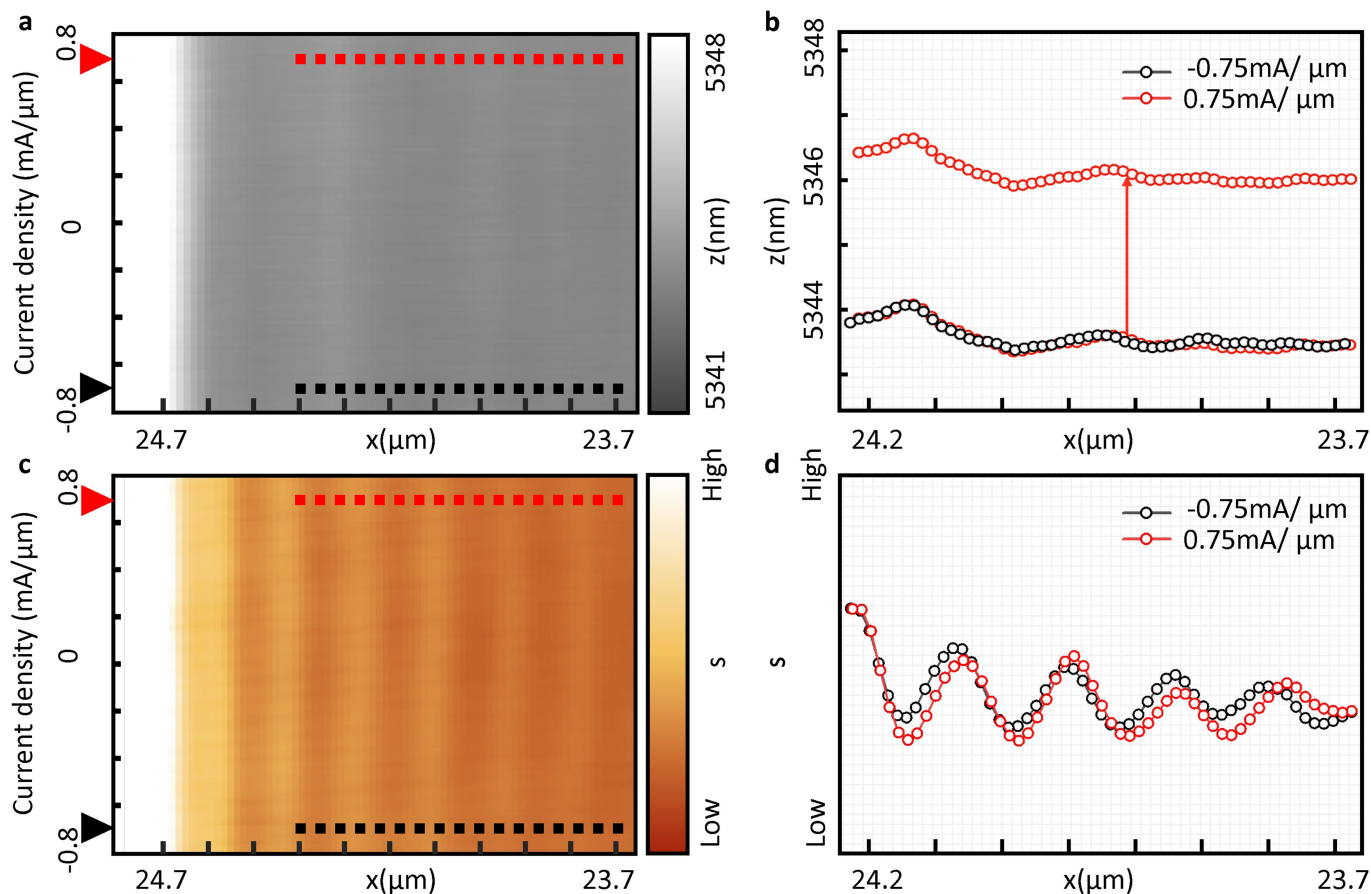
Extended Data Fig. 3 | Current-voltage characteristics of a typical device. The black symbols represent the source-drain voltage while sourcing current through the device. The blue symbols represent the simultaneously measured

voltage on the SPP launcher, representing the current-gating effect induced by the biasing current. Inset shows a magnified view of the low-voltage region.



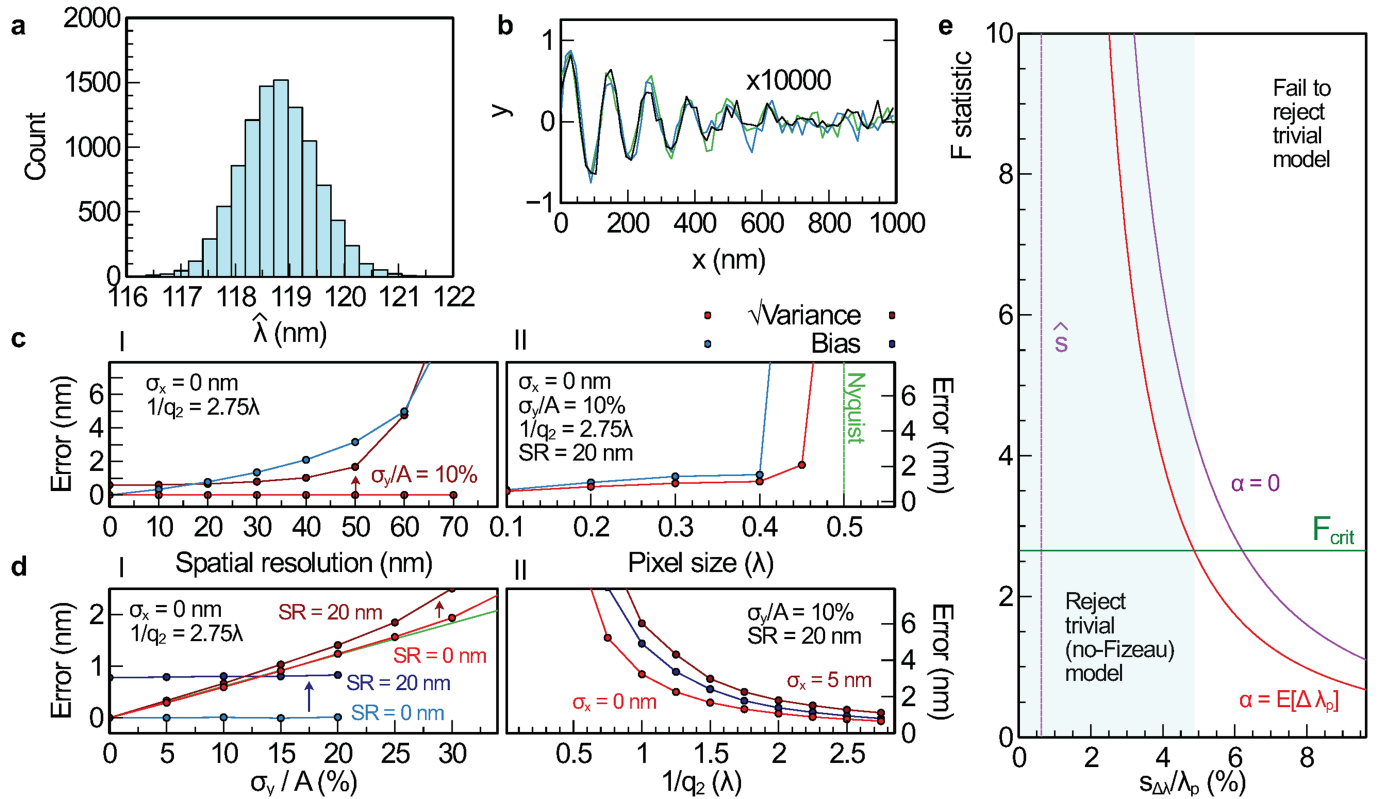
Extended Data Fig. 4 | Characteristic real-space nano-infrared and topography images. **a**, Near-field image taken in the vicinity of a gold launcher at $T=170$ K and $V_g=50$ V. Gold-launched λ_p fringes and tip-launched $\lambda_p/2$ fringes near the graphene edge are clearly visible. Dashed rectangles mark the regions

magnified in **c** and **d**. **b**, AFM topography image taken simultaneously with the near-field image in **a**. The graphene region is uniform with minimal topographic variations. **c**, **d**, Magnified near-field images near graphene edges, showing the tip-launched and edge-reflected SPP fringes with $\lambda_p/2$ periodicity.



Extended Data Fig. 5 | Real-space nano-infrared and topography line profiles under current. **a–d**, Representative results for simultaneously taken topography (**a**, **b**) and near-field (**c**, **d**) data as a function of current density at $T=170$ K and $V_g=-50$ V. **a**, AFM topography collected in the vicinity of a gold launcher on the left of the field of view. The 2D plot is assembled from AFM line profiles measured at different current densities while scanning along the same line in real space. Red and black arrows and dashed lines indicate positions

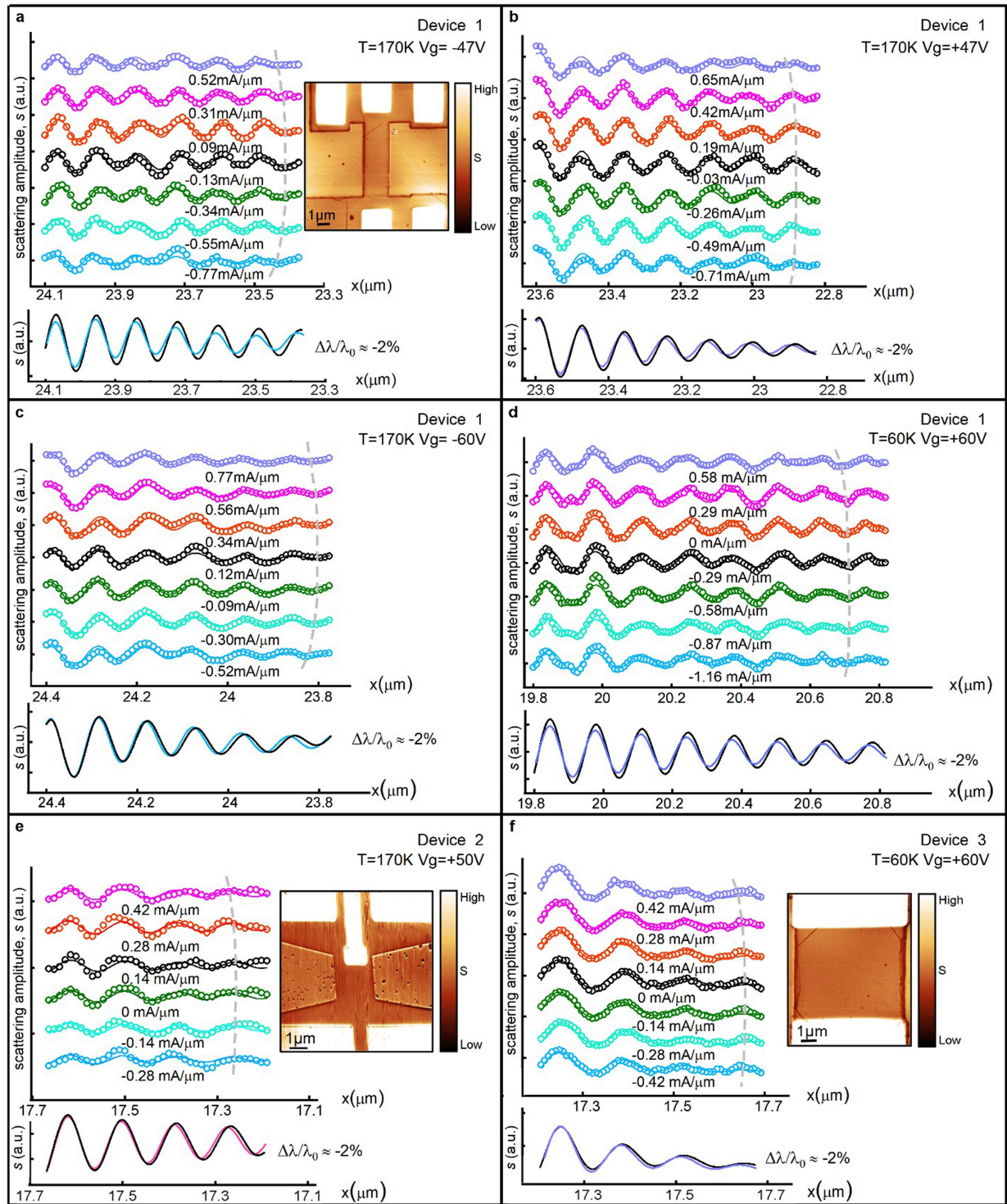
where the averaged line profiles in **b** are acquired. **b**, Averaged line profiles of AFM topography for current densities of ± 0.75 mA μm^{-1} , whose topography signals are essentially the same. One of the line profiles is shifted vertically for clarity. **c**, Near-field data, taken simultaneously with **a**. A standard one-dimensional Fourier filter was applied here to reduce noise. **d**, Averaged line profiles of the near-field signal in **c** for the same current densities as the topography data in **b**. A Fizeau shift is clearly visible.



Extended Data Fig. 6 | Uncertainty analysis for fitted SPP wavelength.

a, Distribution of the least-squares estimate of the SPP wavelength in equation (7) generated by Monte Carlo simulation. **b**, Examples of typical simulated SPP line profiles used for analysis in **a**. **c**, I: Dependence of variance (bright and dark red lines) and bias (blue line) of wavelength estimate on spatial resolution (SR). Bright red line corresponds to zero signal noise ($\sigma_y/A = 0$). Dark red and blue lines correspond to $\sigma_y/A = 10\%$; II: Dependence of bias and variance in wavelength estimate on pixel size in units of wavelength. The pixel size has minimal effect on σ_i as long as one samples above the Nyquist rate, as indicated by the vertical green dashed line. **d**, I: Strong dependence of error in wavelength estimate on signal noise σ_y . The variance of the wavelength estimate (bright red, dark red and green lines) will increase roughly linearly

with σ_y until about 25%, and the bias (bright and dark blue lines) is less than 1 nm for SR = 20 nm; II: Dependence of error in wavelength estimate on SPP propagation length $1/q_2$. Both the variance (bright and dark red lines) and the bias (blue line) of the wavelength estimate improve with $1/q_2$, even more so when there is positioning noise σ_x (dark red line). **e**, Assessing the statistical significance of the Fizeau shift using an F test. Solid red and purple lines represent the dependence of F statistics on the sample wavelength-shift standard deviation $s_{\Delta\lambda}$. Purple line assumes $\alpha = 0$ and red line assumes α is finite (see text). Cyan shaded region corresponds to F statistics that reject the null hypothesis of no Fizeau shift ($F > F_{crit} = 2.65$). Vertical dashed line corresponds to wavelength-shift standard deviation $s_{\Delta\lambda}$ estimated from data in Fig. 3a, b.



Extended Data Fig. 7 | Additional datasets revealing plasmonic Fizeau drag in graphene. Other representative data when scanning along the same line at different d.c. currents (averaged $\pm 25 \mu\text{A} \mu\text{m}^{-1}$ for each profile) for different gate voltages, temperatures and devices. Within a set of polariton line profiles, the first polariton fringes are aligned to enable better visual inspection of Fizeau shifts. Line profiles are shifted vertically for clarity. Within each panel, the

fitted line profiles of the smallest and largest current densities are shown in the lower panel for visual comparison. The images of the devices are near-field scattering amplitude measured at 170 K without gating. **a**, Device 1, $T=170$ K, $V_g=-47$ V; **b**, Device 1, $T=170$ K, $V_g=+47$ V; **c**, Device 1, $T=170$ K, $V_g=-60$ V; **d**, Device 1, $T=60$ K, $V_g=+60$ V; **e**, Device 2, $T=170$ K, $V_g=+50$ V; **f**, Device 3, $T=60$ K, $V_g=+60$ V.

Supplementary information

Fizeau drag in graphene plasmonics

In the format provided by the
authors and unedited

Supplementary Information for “Fizeau Drag in Graphene Plasmonics”

Y. Dong^{1,2†}, L. Xiong^{1†}, I. Phinney³, Z. Sun¹, R. Jing¹, A.S. McLeod¹, S. Zhang¹, S. Liu⁴, F. L. Ruta^{1,2},
H. Gao³, Z. Dong³, R. Pan¹, J.H. Edgar⁴, P. Jarillo-Herrero³, L.S. Levitov³, A.J. Millis¹, M.M. Fogler⁵,
D.A. Bandurin^{3*}, D.N. Basov^{1*}

¹Department of Physics, Columbia University, New York, NY, 10027, USA.

²Department of Applied Physics and Applied Mathematics, Columbia University

³Department of Physics, Massachusetts Institute of Technology, Cambridge, MA, 02139, USA.

⁴The Tim Taylor Department of Chemical Engineering, Kansas State University, Manhattan, KS, 66506, USA.

⁵Department of Physics, University of California San Diego, La Jolla, CA, 92093, USA.

† These authors contributed equally to this work.

* Corresponding authors:

D. Bandurin: bandurin.d@gmail.com

D.N. Basov: db3056@columbia.edu

TABLE OF CONTENTS

Notations	2
Theory of Fizeau plasmon drag in graphene	3
1. Lorentz transforms, drag of light, and drag of plasmons by moving bodies	3
2. Dispersion equation for graphene plasmons in a layered 2d heterostructure	5
3. Optical conductivity and plasmon dispersion of graphene without dc current.....	7
4. Optical conductivity of graphene in the current-carrying state.....	9
5. Analytical results for the Fizeau plasmon drag.....	10
6. Numerical results for the Fizeau plasmon drag	12
7. Remarks on nonlinearities and the Fizeau shift.....	14
Supplementary Table	16
References	17

Notations

32	E^μ	μ th component of the electric field in the stationary frame
33	D	Drude weight
34	η	Drag coefficient of SPP
35	η_ω	Drag coefficient at constant frequency
36	η_q	Drag coefficient at constant momentum
37	H^μ	μ th component of the magnetic field in the stationary frame
38	N_0	Refractive index in the proper (moving) frame
39	N	Refractive index observed in the stationary frame
40	$V(\omega, \mathbf{q})$	Interaction kernel
41	Γ_{ee}	Momentum-conserving quasiparticle scattering rate
42	Γ	Momentum non-conserving quasiparticle scattering rate
43	c	Speed of light
44	f_u	Quasiparticle distribution function
45	f_0	Fermi-Dirac distribution function
46	j^μ	μ th component of the current density in the stationary frame
47	m	Quasiparticle mass
48	n	Quasiparticle density in the stationary frame
49	n_0	Quasiparticle density in the proper (moving) frame
50	p^μ	μ th component of the quasiparticle momentum
51	u	Carrier drift velocity
52	v_F	Fermi velocity
53	v_p	Phase velocity in the stationary frame
54	v_g	Group velocity (g.v.) of light; an auxiliary parameter similar to the g.v. of SPP
55	v_0	Characteristic velocity determining the momentum dependence of $\sigma^{xx}(\omega, \mathbf{q})$
56	q^μ	μ th component of the wave momentum
57	$q_p = q_1 + iq_2$	SPP momentum
58	γ	Lorentz factor (original or quasi)
59	$\epsilon^{\mu\nu}$	Permittivity (dielectric function)
60	$\epsilon_u^{\mu\nu}$	Permittivity (dielectric function) for drift velocity u
61	\mathcal{E}	Quasiparticle energy
62	$\kappa(\omega, \mathbf{q})$	Effective permittivity of the graphene environment
63	λ_p	SPP wavelength
64	μ_u	Auxiliary parameter equal to $\mu_0(u)/\gamma$
65	$\mu_0(u)$	Chemical potential of graphene in the moving (proper) frame
66	ρ	Charge density in the stationary frame
67	ρ_0	Charge density in the proper (moving) frame
68	$\sigma^{\mu\nu}$	Conductivity tensor in the stationary frame
69	$\sigma_u^{\mu\nu}$	Conductivity tensor in the stationary frame for drift velocity u

70 ω Frequency in the stationary frame
 71 ω_0 Frequency in the proper (moving) frame
 72

73 Theory of Fizeau plasmon drag in graphene

74 75 1. Lorentz transforms, drag of light, and drag of plasmons by moving bodies

76 In this subsection we briefly review a few basic facts about the Fizeau light drag effect and
 77 point out its differences from the Fizeau drag of plasmon polaritons (or plasmons to keep it short).
 78 We start with the summary of the Lorentz transformations (LTs) for various physical quantities,
 79 e.g., frequencies and momenta:

$$\omega_0 = \gamma(\omega - uq^x), \quad q_0^x = \gamma\left(q^x - \frac{u}{c^2}\omega\right), \quad q_0^y = q^y. \quad (S1)$$

80 Here the subscript “0” labels quantities measured in the frame moving with velocity u in
 81 the x -direction. The LTs of charge and current density are

$$\rho = \gamma(\rho_0 + uj_0^x/v_F^2), \quad j^x = \gamma(j_0^x + u\rho_0), \quad j^y = j_0^y. \quad (S2)$$

82 We will also need the transformation laws for the electromagnetic (EM) field components:

$$E_0^x = E^x, \quad E_0^y = \gamma\left(E^y - \frac{u}{c}H^z\right), \quad H_0^z = \gamma\left(H^z - \frac{u}{c}E^y\right). \quad (S3)$$

83 The textbook explanation of the Fizeau drag involves nothing more than applying the LT
 84 (S1) to the dispersion equation of light for a medium with a refractive index N_0 :

$$N_0^2(\omega_0)\omega_0^2 - c^2q_0^2 = 0. \quad (S4)$$

85 After a few lines of algebra, one finds that the phase velocity of light $v_p = \omega/q =$
 86 $c/N_0(\omega)$ observed in the stationary frame acquires a u -dependent correction. The drag
 87 coefficient at a given frequency ω is given by

$$\eta_\omega = \left(\frac{\partial v_p}{\partial u}\right)_\omega = \frac{v_p}{v_g}\left(1 - \frac{v_p v_g}{c^2}\right), \quad (S5)$$

88 where $v_g = d\omega/dq = c[d(\omega N_0)/d\omega]^{-1}$ is the group velocity. The drag coefficient at a given
 89 momentum q is defined by

$$\eta_q = \left(\frac{\partial v_p}{\partial u}\right)_q = \frac{v_g}{v_p}\eta_\omega = 1 - \frac{v_p v_g}{c^2}. \quad (S6)$$

90 Equations (S5) and (S6) are valid for light propagating in the direction of motion, where
 91 the drag is the largest. The distinction between the two velocities v_p and v_g can be small in a

weakly dispersive medium such as moving water in Fizeau's experiments. However, for electron systems of interest to us, this distinction is significant. For instance, in a single-component cold plasma (e.g., electron gas) with particle density n , plasma frequency $\omega_p(n) = (4\pi e^2 n/m)^{1/2}$, and optical permittivity $\epsilon(\omega, q = 0) = N_0^2(\omega) = 1 - \omega_p^2/\omega^2$, the group velocity is subluminal $v_g = cN_0 < c$ while the phase velocity is superluminal $v_p = c/N_0 > c$. The product $v_p v_g$ is equal to c^2 , so that the drag is absent^{5,56,57}. By extension, $\eta_\omega = \eta_q = 0$ for solid-state electron plasmas with parabolic quasiparticle dispersion and arbitrary effective mass m , with the role of u played by the drift velocity of the quasiparticles. For a solid with a non-parabolic band dispersion, F_ω is non-vanishing⁷. It is related to the derivative $(\partial N/\partial u)_\omega = -c^{-1}N_0^2\eta_\omega$ of the refractive index with respect to u . Since the drift of quasiparticles in a conductor requires the application of a dc electric field, the Fizeau drag of light is a particular case of the second-order optical nonlinearity. The input spectral parameters of this nonlinear process are $\omega_1 = \mathbf{q}_1 = 0$, $\omega_2 = \omega$, $\mathbf{q}_2 = \mathbf{q}$, and the output parameters are $\omega_3 = \omega$, $\mathbf{q}_3 = \mathbf{q}$. (Henceforth, bold symbols should be understood as either column vectors or matrices.) In general, an order u^k correction to the refractive index is a manifestation of a $(k + 1)^{\text{st}}$ -order nonlinear optical response: schematically, $\text{dc} \times k + \text{ac} \rightarrow \text{ac}$. All such nonlinearities require band non-parabolicity. Actually, free electrons also have a non-parabolic energy-momentum dispersion $\epsilon(p) = c\sqrt{m^2c^2 + p^2}$, so that $\eta_q \sim v_F^2/c^2$ rather than null for electron gas (see Table S1). Here v_F is the Fermi velocity.

In this work, we are interested in the analog of the Fizeau drag for plasmons. The drag coefficients for light and for plasmons can be very different. This is because the dispersion equation for plasmons is $\epsilon(\omega, \mathbf{q}) = 0$ unlike Eq. (S4) for light. Although it is mathematically possible to define a refractive index for plasmons, it is more straightforward to apply the LT (S1) directly to $\epsilon(\omega, \mathbf{q}) = 0$. For example, for the non-relativistic electron gas, neglecting terms $O(v_F^2/c^2)$, one finds $\omega_0 = \omega_p(n_0) = \text{const}$ for the stationary plasma, and so $\omega = \gamma^{-1}\omega_0(n_0) + uq = \gamma^{-3/2}\omega_p(n) + qu$ for the moving plasma. Here $n = \gamma n_0$ is the carrier density measured in the proper frame. [This last relation follows from Eq. (S2) with $j_0^x = 0$.] Hence, the constant- q drag coefficient for plasmons by the electron gas is $\eta_q = 1$ instead of $\eta_q = 0$ for light. In a relativistic plasma or in a solid with non-parabolic band dispersion, we expect $0 < \eta_q < 1$ for plasmons. The case of graphene is a prime example; it is studied in detail in the remaining sections. A summary of Fresnel-Fizeau drag coefficients for some cases can be found in Table S1.

A further insight into the difference between the light drag and the plasmon drag can be gained by exploring the LTs for the longitudinal and transverse permittivities. In fact, the dispersion of light (S4) is determined by the transverse permittivity, while for the plasmon dispersion, $\epsilon(\omega, \mathbf{q})$ in Eq. (S6) is longitudinal. When both \mathbf{q} and \mathbf{u} are in the x -direction, the longitudinal permittivity is simply the xx -component of the full permittivity tensor ϵ . We denote its values in the co-moving and stationary frames by ϵ_0^{xx} and ϵ_u^{xx} , respectively. It is easy to see that the longitudinal permittivity is LT-invariant, $\epsilon_u^{xx}(\omega, \mathbf{q}, n) = \epsilon_0^{xx}(\omega_0, \mathbf{q}_0, n_0)$. Therefore, if ϵ_0^{xx} is equal to zero at frequency ω_0 , then ϵ_u^{xx} is equal to zero at the transformed frequency $\omega =$

$\gamma(\omega_0 + uq^x)$, consistent with the general rule. To prove this statement, we first express the permittivity tensor in terms of the optical conductivity tensor $\sigma(\omega, \mathbf{q})$:

$$\epsilon(\omega, \mathbf{q}) = 1 + \frac{iq^2}{\omega} V(\omega, \mathbf{q}) \sigma(\omega, \mathbf{q}), \quad (\text{S7})$$

where $V(\omega, \mathbf{q}) = 4\pi/q^2$ is the Coulomb kernel. Since the q^2 -factor cancels in Eq. (S7), this equation may appear contrived; however, it will prove useful for the later discussion of two-dimensional (2D) systems. Similar to above, we denote the longitudinal conductivities observed in the co-moving and stationary frames by σ_0^{xx} and σ_u^{xx} , respectively. We can show that

$$\sigma_u^{xx}(\omega, \mathbf{q}, n) = \frac{\omega}{\omega_0} \sigma_0^{xx}(\omega_0, \mathbf{q}_0, n_0). \quad (\text{S8})$$

Indeed, from the charge continuity equation we have $\omega_0 \rho_0 - q_0^x j_0^x = 0$. Substituting this into the second equation in (S2), we obtain $j^x = \frac{\omega}{\omega_0} j_0^x$. In the co-moving frame the system is isotropic, so that the tensor σ_0 is diagonal (we assume no static magnetic field is present). Hence, from Ohm's law $\mathbf{j}(\omega, \mathbf{q}) = \sigma(\omega, \mathbf{q}) \mathbf{E}(\omega, \mathbf{q})$ we get $j_0^x = \sigma_0^{xx} E_0^x$. From Eq. (S3), the x -component of the electric field is invariant; hence, $j_0^x = \sigma_0^{xx} E^x$, which yields Eq. (S8). Finally, substituting Eq. (S8) into (S7), we find $\epsilon^{xx} = \epsilon_0^{xx}$, as stated above.

In contrast, if we consider a transverse EM wave (light) polarized in the y -direction with \mathbf{q} in the x - z plane, then $H_0^z = (cq_0^x/\omega_0)E_0^y$ from the Faraday law and $E^y = (\omega/\omega_0)E_0^y$, $j_y = j_0^y$ from the LTs. Accordingly, the yy -component or “transverse conductivity” transforms as

$$\sigma_u^{yy}(\omega, \mathbf{q}, n) = \frac{\omega_0}{\omega} \sigma_0^{yy}(\omega_0, \mathbf{q}_0, n_0). \quad (\text{S9})$$

Note that the frequency ratio is inverted compared to Eq. (S8). Equation (S9) implies the following transformation law of the refractive index: $(N^2 - 1)\omega^2 = (N_0^2 - 1)\omega_0^2$.

Adding the LT invariant $\omega^2 - c^2 q^2 = \omega_0^2 - c^2 q_0^2$ to both sides, we see that the light dispersion equation (S4) is invariant, as it should be.

As mentioned in the main text, a number of response characteristics of graphene can be understood using relativistic analogies. We will do so below for the plasmon drag by electric current; the equations derived in this subsection will prove useful for this purpose.

2. Dispersion equation for graphene plasmons in a layered 2d heterostructure

Similar to plasmons in bulk media, the dispersion equation for plasmons in graphene embedded in a layered structure is determined by the zeros of the longitudinal permittivity $\epsilon(\omega, \mathbf{q})$. This permittivity is still given by Eq. (S7) but with the 2D version of the Coulomb kernel, $V(\omega, \mathbf{q}) = 2\pi/\kappa q$. In the quasi-static limit $q \equiv |\mathbf{q}| \gg \omega/c$, relevant for our experiments, the effective permittivity $\kappa(\omega, \mathbf{q})$ of the graphene environment is defined based on the condition that the 2D charge density $\rho(t, \mathbf{r}) = e^{i\mathbf{q}^T \mathbf{r} - i\omega t}$ of a propagating plasmon produces

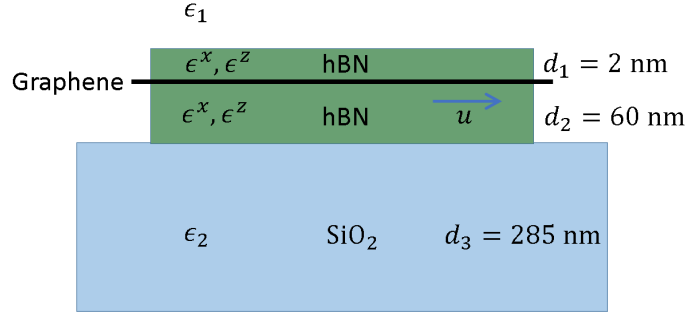


Figure S1. Configuration of the model of graphene encapsulated in hBN.

the scalar potential $\varphi(t, \mathbf{r}) = V(\omega, \mathbf{q})e^{i\mathbf{q}^T \mathbf{r} - i\omega t}$ in the graphene plane, where \mathbf{q}^T is the transpose of \mathbf{q} . Therefore, the plasmon momentum $q_p = q_1 + iq_2$ is the solution of the equation

$$q = \frac{i\omega}{2\pi} \frac{\kappa(\omega, \mathbf{q})}{\sigma^{xx}(\omega, \mathbf{q})}, \quad (\text{S10})$$

which has been established in numerous previous studies (for a review, see⁸). To compute the effective permittivity $\kappa(\omega, \mathbf{q})$, we modeled our experimental device as a 2D heterostructure where graphene is located between two layers of encapsulating material (hBN): a top layer of thickness d_1 and a bottom layer of thickness d_2 . This stack of layers resides on a SiO_2 substrate. We treated hBN as a uniaxial material with in-plane permittivity ϵ^x and out-of-plane permittivity ϵ^z . The permittivity of SiO_2 is ϵ_2 and that of the vacuum above the top hBN layer is ϵ_1 . For this structure, depicted in Fig. S1, an analytical formula for κ is available¹⁸:

$$\kappa(\omega, \mathbf{q}) = \frac{1 - l_1 l_2}{(1 + l_1)(1 + l_2)} \sqrt{\epsilon^x} \sqrt{\epsilon^z}, \quad (\text{S11})$$

where $l_j = r_j e^{2ik^z d_j}$, $k^z = iq\sqrt{\epsilon^x}/\sqrt{\epsilon^z}$, and $r_j = (\sqrt{\epsilon^x} \sqrt{\epsilon^z} - \epsilon_j)/(\sqrt{\epsilon^x} \sqrt{\epsilon^z} + \epsilon_j)$. In the limit $qd_1 \rightarrow 0$, $qd_2 \rightarrow \infty$, Eq. (S11) predicts a momentum-independent effective permittivity $\kappa = (\epsilon_1 + \sqrt{\epsilon^x} \sqrt{\epsilon^z})/2$. For parameters probed in our experiments ($\omega = 890 \text{ cm}^{-1}$, $q \approx 3 \times 10^5 \text{ cm}^{-1}$), the q -dependence of κ , which we calculated numerically using Eq. (S11), is indeed fairly weak:

$$\kappa \approx 2.5, \quad \frac{\partial \ln \kappa}{\partial \ln q} \approx 0.08. \quad (\text{S12})$$

On the other hand, the frequency dependence of $\kappa(\omega, q)$ is significant in and near the lower Reststrahlen band of hBN, $760 < \omega (\text{cm}^{-1}) < 825$.

While knowing κ is important for the quantitative calculation of the plasmon dispersion (see Figs. S2 and S3 below), the physics of the plasmon drag originates from the effect of the carrier drift on the longitudinal conductivity, which is the subject of the following two subsections.

3. Optical conductivity and plasmon dispersion of graphene without dc current

A conventional method of computing the optical conductivity σ_0 in equilibrium is to use the random-phase approximation (RPA). If quasiparticle scattering is neglected and $T = 0$, the RPA yields the following analytical formula for graphene^{58,59,60}:

$$\sigma_0^{xx}(\omega, \mathbf{q}) = \sigma_{0,\mu=0}^{xx} \left[1 + G \left(\frac{\hbar\zeta + 2|\mu_0|}{\hbar v_F q} \right) - G \left(\frac{\hbar\zeta - 2|\mu_0|}{\hbar v_F q} \right) \right] - \frac{2i}{\pi} \frac{e^2 \omega |\mu_0|}{(\hbar v_F q)^2}, \quad (\text{S13.1})$$

$$\sigma_{0,\mu=0}^{xx} = -i \frac{e^2}{4\hbar} \frac{\zeta}{\sqrt{v_F^2 q^2 - \zeta^2}}, \quad \zeta = \omega + i0^+, \quad (\text{S13.2})$$

$$G(x) = -\frac{1}{\pi} \left(x \sqrt{1 - x^2} - \arccos x \right). \quad (\text{S13.3})$$

Here $\mu_0(n_0) = \text{sgn}(n_0) \hbar k_F v_F$ is the graphene Fermi energy, $k_F = |\pi n_0|^{1/2}$ is the Fermi momentum, and n_0 is the quasiparticle density. The RPA formula simplifies considerably if the energy scales $\hbar\omega$ and $\hbar v_F q$ are much smaller than $|\mu_0|$, i.e., in the quasi-classical limit:

$$\sigma_0^{xx}(\omega, \mathbf{q}) = \frac{2D(n_0)}{\pi} \frac{i\omega}{\left(\omega + \sqrt{\omega^2 - v_F^2 q^2} \right) \sqrt{\omega^2 - v_F^2 q^2}} + O \left(\frac{\hbar\omega}{|\mu_0|} \right) \quad (\text{S14})$$

$$= \frac{i}{\pi} \frac{D}{\omega} \left(1 + \frac{v_0^2 q^2}{\omega^2} + \dots \right), \quad v_0 = \frac{\sqrt{3}}{2} v_F, \quad (\text{S15})$$

where $D(n_0) = (e^2/\hbar^2)|\mu_0(n_0)|$ is the Drude weight. Combining Eqs. (S10) and (S13), one arrives at the plasmon dispersion relation in equilibrium:

$$\omega^2(q) = \frac{2D(n_0)}{\kappa} q + v_0^2 q^2 + \dots, \quad q \ll \frac{\omega}{v_F} \ll k_F. \quad (\text{S16})$$

Actually, Eqs. (S14)-(S16) are not specific to graphene; they hold for any isotropic 2D electron gas. This can be seen from an alternative derivation of these results²² via the Boltzmann kinetic equation (BKE) for the quasiparticle distribution function $f(\mathbf{p}) = f_0(\mathbf{p}) + \delta f(\mathbf{p}) e^{i\mathbf{q}^T \mathbf{r} - i\omega t}$ in the presence of a perturbing in-plane electric field $\mathbf{E}(\omega, \mathbf{q}) e^{i\mathbf{q}^T \mathbf{r} - i\omega t}$:

$$i(\mathbf{q}^T \mathbf{v}(\mathbf{p}) - \omega) \delta f(\mathbf{p}) - e \mathbf{E}^T(\omega, \mathbf{q}) \nabla_{\mathbf{p}} f_0(\mathbf{p}) = I, \quad f_0(\mathbf{p}) = \frac{1}{e^{(\varepsilon(\mathbf{p}) - \mu)/k_B T} + 1}. \quad (\text{S17})$$

Here $\varepsilon(\mathbf{p})$ is the energy of a quasiparticle with momentum \mathbf{p} and $\mathbf{v}_{\mathbf{p}} = \nabla_{\mathbf{p}} \varepsilon(\mathbf{p})$ is its velocity, and \mathbf{q}^T means the transpose of the vector \mathbf{q} such that its product with another vector gives their inner product. In graphene, one is to use $\varepsilon(\mathbf{p}) = \text{sgn}(\mu) v_F |\mathbf{p}|$. If the collision integral $I = I[f]$ is set to zero, then $\delta f(\mathbf{p}) = i e \mathbf{E}^T \nabla_{\mathbf{p}} f_0(\mathbf{p}) / (\omega - \mathbf{q}^T \mathbf{v}_{\mathbf{p}})$, from which Eq. (S14) follows easily.

The BKE becomes the method of choice if quasiparticle scattering is important. Two types of processes should be distinguished. First, quasiparticles in graphene can interact with impurities and phonons. We estimate the corresponding scattering rate Γ to be relatively small, perhaps a fraction of a THz because of the high quality of the 2D materials in our device and because of the suppression of electron-phonon scattering at the measurement temperature $T \sim 170$ K. If $\omega \gg v_F q$, which is the case for plasmons, qualitatively correct results are obtained by including Γ via the relaxation-time approximation $I[f] \sim -\Gamma \delta f$. This leads to the replacement of ω by $\omega + i\Gamma$ in Eq. (S14). Accordingly, in the frequency range of interest, $\omega \gg \Gamma$, this scattering mechanism affects $q_2 = \text{Im } q_p$ but not $q_1 = \text{Re } q_p$, i.e., it modifies the damping rather than the dispersion of the plasmons.

Another source of scattering is electron-electron interaction. The electron-electron scattering rate can be estimated as $\Gamma_{ee} \sim T^2/|\mu_0| \sim 1$ THz, which is higher than Γ . The collisionless approximation used to derive Eqs. (S16) and (S17) is justified only if the inequality $\omega \gg \Gamma_{ee}, \Gamma$ is satisfied. On the other hand, this approximation becomes questionable in the so-called hydrodynamic regime $\Gamma \ll \omega \ll \Gamma_{ee}$ where electron-electron interaction causes quasiparticles to behave collectively, as a fluid^{26,27,31}. It is instructive to review the response of graphene in this regime because one can argue that it is not too far from our experimental frequency range.

Theoretical analysis of the hydrodynamic regime involves solving the equations of motion for collective variables, such as local density $n(t, \mathbf{r})$ and flow velocity $\mathbf{u}(t, \mathbf{r})$. These equations can be derived from the BKE, assuming the local quasiparticle distribution function is constrained to be in the form

$$f_u(\mathbf{p}) = \frac{1}{e^{(\varepsilon(\mathbf{p}) - \mathbf{u}^T \mathbf{p} - \mu_u)/k_B T} + 1},$$

for which the collision integral $I[f_u]$ vanishes. For classical fluids, the change from $f_0(\mathbf{p})$ to $f_u(\mathbf{p})$ can be considered a Galilean transformation. However, a more physically and mathematically appealing picture of the electron hydrodynamics of graphene is developed if it is modeled instead after relativistic fluids, with the speed of light replaced by v_F . This is because i) admissible drift velocities for which $f_u(\mathbf{p})$ is integrable are restricted to $u < v_F$ and ii) for such u the Dirac dispersion of quasiparticles is invariant under the quasi-Lorentz transformations (QLT)

$$\varepsilon_0(\mathbf{p}) = \gamma(\varepsilon(\mathbf{p}) - u p^x) = \varepsilon(\mathbf{p}_0), \quad p_0^x = \gamma \left(p^x - \frac{u}{v_F^2} \varepsilon(\mathbf{p}) \right), \quad p_0^y = p^y. \quad (\text{S18})$$

From here onwards, $\gamma = (1 - u^2/v_F^2)^{-1/2}$ is the *quasi*-Lorentz factor introduced in the main text. Unfortunately, the collision integral in the BKE is not invariant under the QLT for the realistic Coulomb interaction. However, it would be invariant if the interaction were short-range. Therefore, relativistic hydrodynamics can be a good approximation for graphene if the short-range part of the interaction is strong enough to enforce local equilibrium but not so strong as to

alter the basic thermodynamic equation of state. Additionally, the macroscopic EM field created by the long-range tail of the Coulomb interaction must be treated using the usual Lorentz transformation (LT), which reduces to the Galilean one in the quasi-static case. In other words, one has to use a hybrid approach: QLT for matter, LT for the EM field. Note that the Coulomb interaction kernel $V(\omega, \mathbf{q}) = 2\pi/\kappa q$ can, in principle, be controlled experimentally through engineering of the graphene environment and its effective permittivity $\kappa(\omega, \mathbf{q})$ (Sec. 2). Finally, corrections to the hydrodynamic approximation do exist and they scale as $1/\Gamma_{ee}$.

For the equilibrium longitudinal conductivity, the hydrodynamic theory plus a first such correction gives the formula

$$\sigma_0^{xx}(\omega, \mathbf{q}) = \frac{i}{\pi} \frac{D_h \omega}{\omega^2 - v_d^2 q^2} + \frac{D - D_h}{\pi \Gamma_{ee}}, \quad (\text{S19})$$

where $D_h = D_h(n_0, T)$ is a “hydrodynamic” Drude weight (Ref.31 and references therein). At temperatures $\ll |\mu|$, which is our experimental situation, D_h approaches the usual Drude weight D . Therefore, at $q \ll \omega/v_F$, the expressions for the conductivity and the plasmon dispersion differ from Eqs. (S15) and (S16) only in the coefficient for the q^2 term. Specifically, v_0 gets replaced by v_d , the velocity of a sound-like collective mode (referred to as the energy wave or demon³¹), which is equal to $v_F/\sqrt{2}$ for weak Coulomb interaction. The alteration of the q^2 term can be traced to the different shapes of the Fermi surface perturbation caused by the electric field in the two regimes. In the hydrodynamic case, the displacement of the Fermi surface is angle-dependent; in the collisionless one, it is a rigid shift.

By inversion symmetry, the leading momentum-dependent correction to the conductivity should always be quadratic. Therefore, Eq. (S16) should be valid for any relation between ω and Γ_{ee} as long as we use the correct $v_0 = v_0(\omega)$. If desired, an interpolation formula for $v_0(\omega)$ can be derived following Ref. 31. We expect that v_0 monotonically increases as frequency increases and the system behavior evolves from hydrodynamic to collisionless^{20,22}. We will see that v_0 affects the plasmon drag coefficient later.

4. Optical conductivity of graphene in the current-carrying state

We proceed to examine the plasmonic response of graphene with a uniform dc current. Assuming $\Gamma_{ee} \gg \Gamma$, the steady state can be approximated by a hydrodynamic flow with the quasiparticle distribution function in the form

$$f_u(\mathbf{p}) = \frac{1}{e^{(\varepsilon(\mathbf{p}) - \mathbf{u}^T \mathbf{p} - \mu_u)/T} + 1} = \frac{1}{e^{(\varepsilon(\mathbf{p}_0) - \mu_0)/\gamma T} + 1},$$

where $\varepsilon(\mathbf{p}_0)$ is given by Eq. (S18). The choice of the “proper” chemical potential μ_0 in this expression must preserve the quasiparticle density n , which remains fixed by the gate voltage in our experiment. In other words, n is independent of u , while the quasiparticle density in the “proper frame,” $n_0 = n/\gamma$ (see Sec. 1), is a mathematical construct that varies with u . The situation is opposite to Fizeau’s experiments where the density n_0 in the proper frame was a

physical constant. For non-degenerate quasiparticle gas in graphene we have $|n_0| \propto \mu_0^2$, so that the appropriate choice of μ_0 for us is $\mu_0(u) = \mu_0(0)/\gamma^{1/2}$ and $\mu_u = \mu_0(u)/\gamma = \mu_0(0)/\gamma^{3/2}$.^[61]

Let us discuss the “longitudinal conductivity” σ_u^{xx} in the current-carrying state, starting with the collisionless limit. In this limit $\omega \gg \Gamma, \Gamma_{ee}$, and so we can ignore both scattering rates. To find σ_u^{xx} , one can solve the BKE (S17) using the ansatz $f(\mathbf{p}) = f_u(\mathbf{p}) + \delta f(\mathbf{p})e^{i\mathbf{q}^T \mathbf{r} - i\omega t}$. For $\mathbf{q} \parallel \mathbf{u} \parallel \hat{\mathbf{x}}$, the result is²²

$$\sigma_u^{xx}(\omega, \mathbf{q}) = \frac{2D(n_0)}{\pi} \frac{i\omega}{\left[\gamma(\omega - uq) + \sqrt{\omega^2 - v_F^2 q^2} \right] \sqrt{\omega^2 - v_F^2 q^2}}. \quad (\text{S21})$$

Comparing with Eq. (S10), we see that (S21) is consistent with Eq. (S8). [Note that $\omega_0^2 - v_F^2 q_0^2 = \omega^2 - v_F^2 q^2$.] For the convenience of the reader, we reproduce Eq. (S8) together with the subsidiary QLT expressions below:

$$\begin{aligned} \sigma_u^{xx}(\omega, \mathbf{q}, n) &= \frac{\omega}{\omega_0} \sigma_0^{xx}(\omega_0, \mathbf{q}_0, n_0), \\ \omega_0 &= \gamma(\omega - uq), \quad q_0 = \gamma \left(q - \frac{u}{c^2} \omega \right), \quad n_0 = \frac{n}{\gamma}. \end{aligned} \quad (\text{S8}')$$

A small- u approximation to this equation was previously derived⁶² by means of a Galilean transformation $\omega_0 = \omega - uq$ (i.e., neglecting the difference between γ and unity). We see now that the transformation rule (S8') obtained by the QLT extends the validity of this formula to an arbitrary drift velocity $u < v_F$. The reasons why the QLT works are as follows: i) we are assuming that the steady-state distribution $f_u(\mathbf{p})$ is the QLT of the equilibrium one, $f_0(\mathbf{p})$. The condition $\Gamma_{ee} \gg \Gamma$ is crucial for this unless u/v_F is small; ii) we are assuming that the electric field $\mathbf{E}(\omega, \mathbf{q})$, the momentum \mathbf{q} , and the drift velocity \mathbf{u} are all aligned, which makes the field invariant not only under the true transformation law (S3) but also under the QLT; and finally, iii) the left-hand side of the BKE (S17) is invariant under the QLT. Under these assumptions, Eq. (S8') applies in the hydrodynamic regime as well, so that no separate derivation for that regime is needed.

5. Analytical results for the Fizeau plasmon drag

Combining Eqs. (S8'), (S10), and (S15), we arrive at the plasmon dispersion equation

$$\omega_0^2 \simeq \frac{2D(n_0)q}{\kappa(\omega, q)} + v_0^2 q_0^2, \quad (\text{S22})$$

where ω_0 and q_0 are defined in the second row of Eq. (S8'). For a given q , Eq. (S22) is quadratic in ω , so the solution is easy to find:

$$\omega \simeq \left(1 - \frac{v_0^2 u^2}{v_F^4} \right)^{-1} \left[\eta u q + \sqrt{\left(1 - \frac{v_0^2 u^2}{v_F^4} \right) \Omega^2 + (\eta u q)^2} \right]. \quad (\text{S23.1})$$

286 Here Ω^2 and F stand for

$$\Omega^2 = \left(1 - \frac{u^2}{v_F^2}\right) \frac{2D(n_0)}{\kappa} q + (v_0^2 - u^2)q^2, \quad (\text{S23.2})$$

$$\eta(\omega) = 1 - \frac{v_0^2}{v_F^2} = \begin{cases} 1/4, & \text{massless, } \omega \gg \Gamma_{ee}, \\ 1/2, & \text{massless, } \omega \ll \Gamma_{ee}, \\ 1, & \text{parabolic band.} \end{cases} \quad (\text{S23.3})$$

287 Expanding Eq. (S23.1) to the second order in u , we arrive at

$$\omega \simeq \sqrt{\frac{2D(n)q}{\kappa(\omega, q)}} \left[1 - \frac{1}{2} \left(\eta + \frac{1}{4} \right) \frac{u^2}{v_F^2} \right] + \eta u q. \quad (\text{S24})$$

288 The constant $\frac{1}{4}$ inside the square brackets compensates for the switch from n_0 to $n = \gamma n_0$ in the
 289 argument of the function $D(n) \propto |n|^{1/2}$, as discussed above. In comparison, Ref.22 gives the
 290 following result (in our notations):

$$\omega = \sqrt{\frac{2\gamma}{\gamma + 1}} \sqrt{\frac{2D(n_0(\mu_u))}{\kappa(\omega, q)}} q + \frac{1}{2} \frac{\gamma}{\gamma + 1} u q + O(q^{3/2}), \quad (\text{S25})$$

291 which agrees with Eq. (S24) if we recall that $\mu_u = (\mu_0(0)) / \gamma^{3/2}$ (Sec. 4) and use $\eta = 1/4$, which
 292 is appropriate for the collisionless limit. Equation (S25) can be obtained by combining Eq. (S10)
 293 with Eq. (S21) expanded to the second order in q . The Fizeau plasmon drag effect we have sought
 294 to analyze is the difference between the plasmon dispersion Eq. (S24) for the drifting electrons
 295 and Eq. (S16) for the equilibrium state. For example, we see that the linear correction to the
 296 plasmon phase velocity is ηu , so that η plays the role of the drag coefficient (hence, the notation).
 297 The $O(u^2)$ term inside the square brackets represents an effective reduction of the Drude weight.
 298 As mentioned in Sec. 1, it can be understood as the third-order optical nonlinearity. For graphene
 299 in a hydrodynamic regime, the third-order optical conductivity at arbitrary input frequencies was
 300 computed recently in Ref. 63. Equation (23) therein agrees with Eq. (S24) in the appropriate limit.

301 Note that a derivation of the plasmon drag effect can also be done, with minimal changes,
 302 for massive Dirac fermions with energy dispersion $\varepsilon(\mathbf{p}) = c\sqrt{m^2c^2 + p^2}$. In a d -dimensional
 303 degenerate free Fermi gas in a collisionless regime, we find $v_0^2 = \frac{3}{d+2} v_F^2$, which leads to the
 304 formula $\eta_q = 1 - \frac{3}{5} \frac{v_F^2}{c^2}$ in Table S1. For Fermi energies near the bottom of the band, where it is
 305 nearly parabolic, the Fermi velocity and hence the characteristic velocity v_0 are much smaller
 306 than c . In this “non-relativistic” limit, the drag coefficient η_q approaches unity [Eq. (S23.3), last
 307 row] while the Drude weight exhibits no reduction^{6,7,30,64,65} because of the restored Galilean
 308 invariance. Conversely, the reduction of the drag coefficient η below unity and the existence of

the nonlinear-in- u frequency shift in Eq. (S24) are manifestations of a broken Galilean invariance in graphene.

In the experiment, ω is fixed and the shift $\Delta q(u)$ of the plasmon momentum is measured. Therefore, for comparison between theory and experiment, we need to solve for Δq from Eq. (S22). This is similar to the transition from Eq. (S5) to Eq. (S6). Keeping only the terms up to $O(u^2)$, the result is

$$\frac{\Delta q}{q} \simeq -\frac{\eta u}{v_g} + \frac{1}{2} \left(\eta + \frac{1}{4} \right) \frac{v_p}{v_g} \frac{u^2}{v_F^2}, \quad v_g = \frac{v_p}{2} \left(1 + \frac{v_0^2}{v_p^2} \right) - \frac{v_p}{2} \left(1 - \frac{v_0^2}{v_p^2} \right) \frac{\partial \ln \kappa}{\partial \ln q}, \quad (\text{S26})$$

where $v_p = \omega/q$ is the plasmon phase velocity, $v_g = \partial \omega_{\text{rhs}} / \partial q$, and ω_{rhs} stands for the square-root of the right-hand side of Eq. (S22). (If κ were frequency-independent, v_g would be equal to the plasmon group velocity $d\omega/dq$.) For the shift of the plasmon wavelength, we obtain

$$\frac{\Delta \lambda_p}{\lambda_p} \simeq \frac{\eta u}{v_g} - \frac{1}{2} \left(\eta + \frac{1}{4} \right) \frac{v_p}{v_g} \frac{u^2}{v_F^2}. \quad (\text{S27})$$

In the $O(u^2)$ terms in Eqs. (S26), (S27), we neglected quantities containing the small parameter $v_0 q / \omega = v_0 / v_p \ll 1$ because such terms are already neglected in Eq. (S22).

We can do quick estimates for our experimental situation, where the plasmon phase velocity is $v_p = 3.2 v_F$, the logarithmic derivative of κ is numerically small [Eq. (S12)], and $\eta = \frac{1}{4}$, so that $v_g \approx v_p/2$. The ratio of the quadratic and linear corrections in $\Delta \lambda_p$ is then of the order of $3.2u/v_F$. For our highest quasiparticle drift velocities $u \sim 0.17 v_F$, the quadratic correction is significant. This suggests that a numerical solution of the dispersion equation may be in order. We will discuss this solution in the next subsection.

6. Numerical results for the Fizeau plasmon drag

In this subsection we present our numerical solutions of Eq. (S22). The calculated plasmon dispersions are shown in the left panel of Fig. S2. The dispersion has a complicated shape because of the frequency-momentum dependence of the effective permittivity $\kappa(\omega, \mathbf{q})$. The dispersion is broken into two branches, one above and one below the Reststrahlen band of hBN. Our experiments are done at frequency $\omega = 890 \text{ cm}^{-1}$, which belongs to the upper branch. At this frequency, $\kappa \approx 2.5$ and slowly varies with ω , so that the canonical $\omega \propto \sqrt{q}$ form of the 2D plasmon spectra is approximately restored. Fig. S2 demonstrates a systematic deformation of these spectra as u increases first to $0.2 v_F$, which is still practical, and then to $0.5 v_F$, which is challenging to achieve experimentally. To show the carrier drift-induced shift of the plasmon wavelength $\Delta \lambda_p$ more clearly, we plotted it in the right panel of Fig. S2. The curve labeled “Kinetic” was calculated using $v_0 = \frac{\sqrt{3}}{2} v_F$ in Eq. (S22), the one labeled “Hydrodynamic” is for $v_0 = \frac{\sqrt{2}}{2} v_F$, and the one labeled “Galilean” is for a system that has a parabolic band dispersion and the same

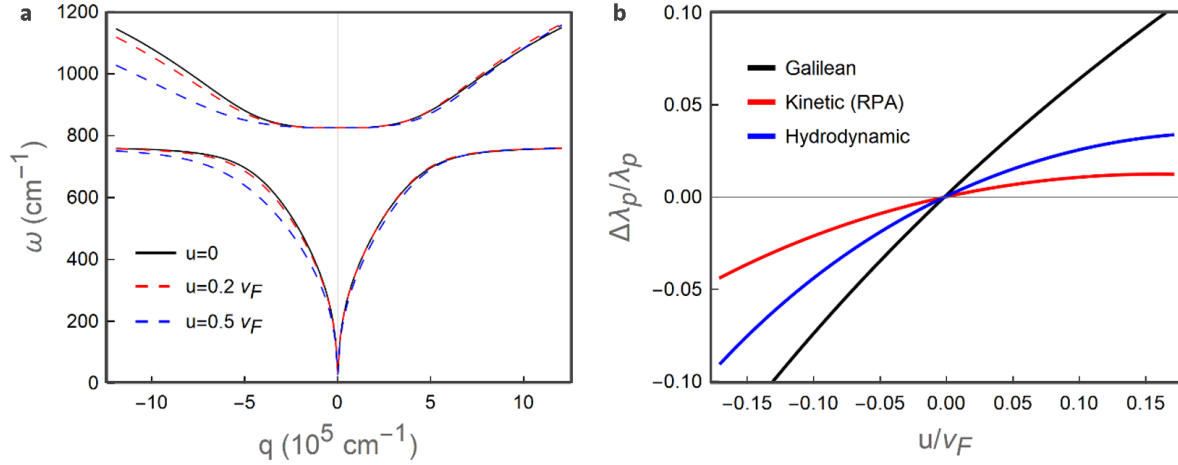


Figure S2. *a*, The plasmon dispersion of the heterostructure shown in Fig. S1 with and without the dc current. *b*, The wavelength shift as a function of drift velocity at $\omega = 890 \text{ cm}^{-2}$. Red (blue) curve is calculated assuming the system is in the collisionless (hydrodynamic) regime. Black curve is for an electron system with a parabolic band dispersion, for comparison (see text). The carrier density is $n = 2.88 \times 10^{12} \text{ cm}^{-2}$.

carrier density and Fermi velocity. In agreement with the estimate in Sec. 5, the “Hydrodynamic” and especially the “Kinetic” curves become visibly nonlinear at $|u| \sim 0.1 v_F$.

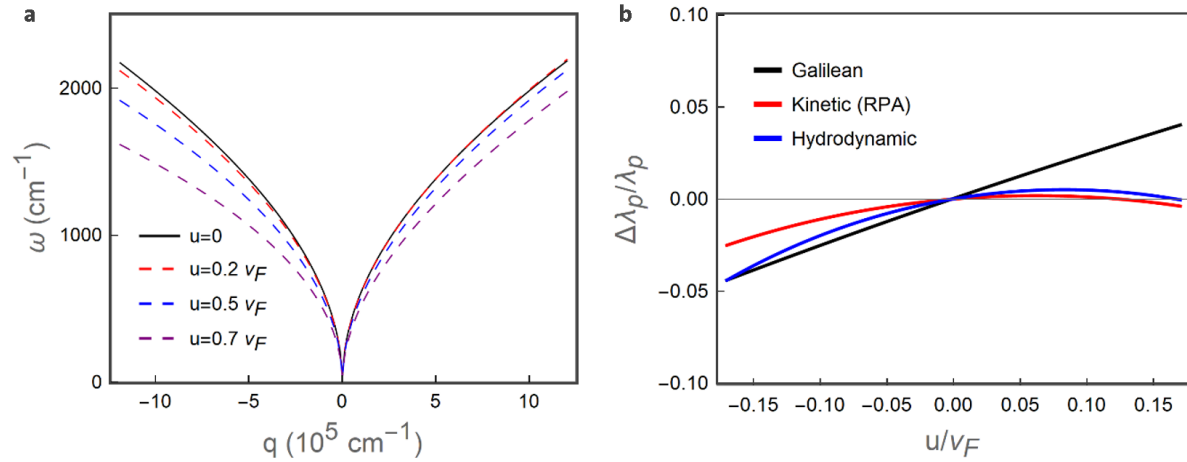


Figure S3. *a*, The plasmon dispersion of free-standing graphene ($\kappa = 1$). *b*, The wavelength shift as a function of drift velocity for the plasmon at frequency $\omega = 890 \text{ cm}^{-2}$. Due to the third-order nonlinear optical effect present already at moderate u , the frequency is down-shifted for plasmons propagating in both directions. The doping level is $n = 2.88 \times 10^{12} \text{ cm}^{-2}$.

Figure S3 illustrates the effect of the environment on the Fizeau drag. It shows the results of the calculations done for the vacuum value $\kappa = 1$ of the effective permittivity. In that case, there is no Reststrahlen band and no gap in the plasmon spectrum. The plasmon wavelength is larger because for the same frequency and doping, it scales as $\lambda_p \propto \kappa^{-1}$. As a result, the drift-induced wavelength shift $\Delta\lambda_p/\lambda_p$ is smaller and the onset of nonlinear behavior occurs at smaller u than for the hBN-encapsulated graphene.

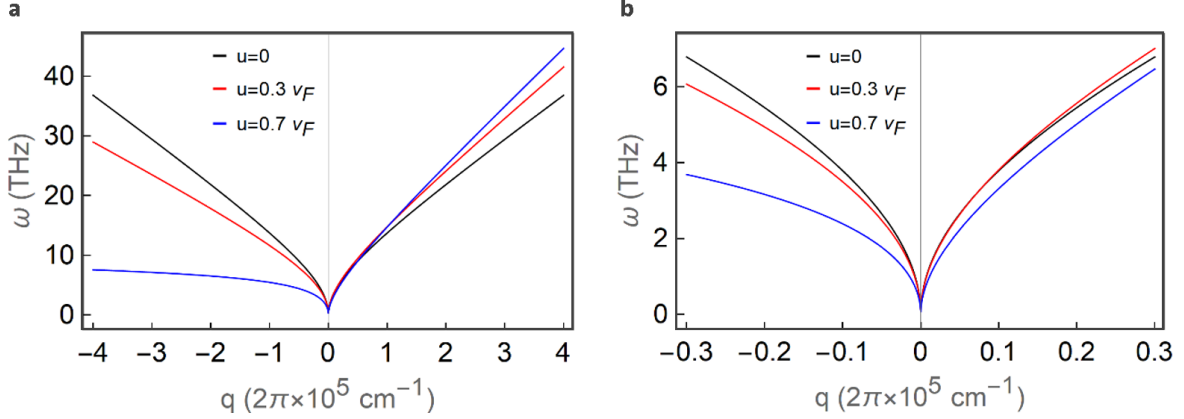


Figure S4, The plasmon (demon, Sec. 3, assumed in the hydrodynamic regime) dispersion of free-standing graphene ($\kappa = 1$) with a small doping, $\mu_0 = 13 \text{ meV}$, $n = 1.2 \times 10^{10} \text{ cm}^{-2}$. Right panel shows the enlarged low frequency-momentum part of the left panel.

Figure S4 shows the effect of bringing the system close to the Dirac point where the Drude weight is greatly reduced and the plasmon frequency-momentum dispersion is much closer to the linear law, except at low q . In the former, linear dispersion regime, the plasmons co-propagating with the flow have a higher phase velocity, while counter-propagating plasmons have a lower velocity, consistent with Ref. 20. In the latter, low-momentum region, shown in the right panel of Fig. S4, we have the $\omega \propto \sqrt{q}$ dispersion. At large enough u , the plasmon frequency is reduced below its equilibrium value for either plasmon propagation direction.

7. Remarks on nonlinearities and the Fizeau shift

Here we clarify two different notions of nonlinearity that are both relevant to the results and analysis reported in the manuscript. The first one is the general notion of optical nonlinearity. The second is the notion of nonlinearity pertaining to the amount of Fizeau shift prompted by dc current as in Eq. (1) of the main text. As stated in the main text, these two notions can be translated into each other.

We begin with the general notion of optical nonlinearity. The net plasmonic response is caused by two electric fields: one is the inhomogeneous near field $E_{ac}(\omega)$ at frequency ω emitted by the gold antenna, and the other is the dc electric field $E_{dc}(0)$ from the source/drain that pushes the static current. Therefore, the linear Fizeau shift is itself a manifestation of the second order nonlinearity³¹ in the response current $\sigma^{(2)} E_{dc} E_{ac}(\omega)$. This term is nonzero due to the inhomogeneity of $E_{ac}(\omega)$. Given a fixed dc current, the plasmons are in linear response to the inhomogeneous $E_{ac}(\omega)$. Therefore, they have fixed Fizeau shift $\frac{d\lambda_p}{\lambda_p}$ everywhere. Nonlinear effects in $E_{ac}(\omega)$ can occur for stronger excitations. The second-order effect in $E_{ac}(\omega)$ will cause a signal at 2ω , inaccessible in our experiments. Going to an even higher order, the third-order effect in $E_{ac}(\omega)$ can indeed result in different plasmon wavelengths at different locations relative to the antenna. However, this effect occurs for very strong fields: $E_{ac}(\omega) > E_c \sim \frac{\omega \hbar k_F}{e} \sim$

372 $3 \times 10^5 \text{ V/cm}$ at our doping level (see Ref. 60), far beyond the field regime of our experiment.
373 Note that electrostatic doping (e.g., the electrostatic field that introduces carriers into a device)
374 can obviously affect an ac plasmonic response. This effect is usually not referred to as an optical
375 nonlinearity because its effect on ac response is often nonperturbative. However, our static
376 current-driven situation is different in that we can expand the plasmonic response strictly in
377 powers of the dc electric field that causes the dc flow, making the analogy to nonlinear optics
378 appropriate.

379 We next address the notion of nonlinearity pertaining to the amount of Fizeau shift
380 prompted by dc current as in Eq. (1) of the main text (Eq. S27). In that equation, the $O(u^2)$ term
381 is formally described a “second-order Fizeau shift”. Put in the broad context of nonlinearities
382 discussed in the previous paragraph, the $O(u^2)$ term can be viewed as a third-order nonlinear
383 optical effect: the plasmons are impacted by the product $\sigma^{(3)} E_{\text{dc}}^2 E_{\text{ac}}(\omega)$. This “second-order
384 Fizeau shift” can be understood by noting that at order $O(u^2)$, the dc current flow reduces the
385 effective Drude weight for AC conductivity. The reduction is because the third-order nonlinear
386 optical conductivity $\sigma^{(3)}$ is negative in graphene due to the Dirac dispersion of electrons⁶³.

Supplementary Table

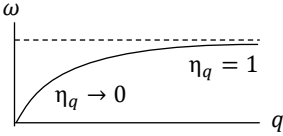
EM mode	Material class	Linear drag coefficient η_q	Comment	Source or Reference No.
Light	Simple dielectric	$1 - \frac{v_p^2}{c^2}$	$v_p = v_g$	[1]
	Dispersive dielectric	$1 - \frac{v_p v_g}{c^2}$		[66]
	Degenerate 3D electron gas	$\frac{2}{5} \frac{v_F^2}{c^2} \frac{\omega_p^4}{\omega^4}$	$\epsilon^{yy} = 1 - \frac{\omega_p^2}{\omega^2} \left(1 - \frac{2}{5} \frac{v_F^2 q^2}{\omega^2}\right)$	This work
	Metal with a non-parabolic band dispersion	$\frac{2}{5} \frac{\omega_p^2}{\omega^2} \left(\frac{k_F}{v_F} \frac{dv_F}{dk_F} - 1\right)$	$O(v_F^0/c^0)$	[7]
Plasmon or SPP	Degenerate 3D electron gas	$1 - \frac{3}{5} \frac{v_F^2}{c^2}$	$\epsilon^{xx} = 1 - \frac{\omega_p^2}{\omega^2} \left(1 - \frac{3}{5} \frac{v_F^2 q^2}{\omega^2}\right)$	This work
	Metal-dielectric interface	$\simeq 1 \quad q \gg \frac{\omega_p}{c}$ $\ll 1 \quad q \ll \frac{\omega_p}{c}$		[23]
	2D electron gas	$\simeq 1$	$O(v_F^2/c^2)$ terms ignored	2D version of [67]
	Graphene	$1 - \frac{v_0^2}{v_F^2}$	$\frac{1}{4} < \eta_q < \frac{1}{2}$	[20],[21], [22], and this work

Table S1. Characteristics of Fresnel-Fizeau drag of light and plasmons in common classes of materials.

-
- ⁵⁶ Landau, L. D. and Lifshitz, E. M. *Electrodynamics of Continuous Media*. (Elsevier, 1984).
- ⁵⁷ Jones, R. Radiation pressure and ‘aether drag’ in a dispersive medium. *Nature* **277**, 370 (1979).
- ⁵⁸ Wunsch, B., Stauber, T., Sols, F. & Guinea, F. Dynamical polarization of graphene at finite doping. *New J. Phys.* **8**, 318 (2006).
- ⁵⁹ Hwang, E. H. & Das Sarma, S. Dielectric function, screening, and plasmons in two-dimensional graphene. *Phys. Rev. B* **75**, 205418 (2007).
- ⁶⁰ Fei, Z. et al. Gate-tuning of graphene plasmons revealed by infrared nano-imaging. *Nature* **487**, 82-85 (2012).
- ⁶¹ This entails $n = \gamma^3 n_0(\mu_u)$, in agreement with Ref. 22 (Duppen et al.).
- ⁶² Morgado, T. A. & Silveirinha, M. G. Negative Landau damping in bilayer graphene, *Phys. Rev. Lett.* **119**, 133901 (2017).
- ⁶³ Sun, Z., Basov, D. N. & Fogler, M. M. Third-order optical conductivity of an electron fluid. *Phys. Rev. B* **97**, 075432 (2018).
- ⁶⁴ Súilleabháin, L. C. Ó. et al. Raman studies of plasmon modes in a drifting two-dimensional electron gas. *J. Appl. Phys.* **76**, 1701-1705 (1994).
- ⁶⁵ Bhatti, A. S. et al. Plasmon dispersion and electron heating in a drifting two-dimensional electron gas. *Phys. Rev. B* **51**, 2252-2258 (1995).
- ⁶⁶ Lorentz, H. A., *Versuch einer Theorie der elektrischen und optischen Erscheinungen in bewegten Körpern*, p. 101. (Brill, Leiden, 1895).
- ⁶⁷ Lifshitz, E. M. & Pitaevskii, L. P. *Physical Kinetics*, Sec. 61 (Elsevier, New York, 1981).